https://doi.org/10.5194/essd-2026-732
Preprint. Discussion started: 2 November 2026
© Author(s) 2026. CC BY 4.0 License.



Open Access Earth System Science Data Discussions

A long-term gridded dataset of the vegetation–atmosphere decoupling coefficient across the contiguous United States, 1982–2020

Jinran Xiong[1,2], Han Chen[3], Wenli Zhao[4], Ziqi Lin[2], Chunmiao Zheng[2], Yu Feng[2*]

Affiliations:

[1] Department of Environmental Science and Engineering, University of Science and Technology of China, Hefei 230026, China

[2]School of the Environment and Sustainable Engineering, Eastern Institute of Technology, Ningbo 315200, China

[3]Institute of Surface-Earth System Science, School of Earth System Science, Tianjin University, Tianjin 300072, China

[4]Department of Earth and Environmental Engineering, Columbia University, New York, NY, USA

*Correspondence: yufeng@eitech.edu.cn (Y. Feng)

https://doi.org/10.5194/essd-2026-732
Preprint. Discussion started: 2 November 2026
© Author(s) 2026. CC BY 4.0 License.



Open Access Earth System Science Data Discussions

Abstract

Terrestrial evapotranspiration (ET) is widely mapped as a flux, but the vegetation–atmosphere coupling regime that regulates it, commonly summarized by the decoupling coefficient (Ω), is rarely represented in gridded data products. Existing Ω estimates are largely restricted to flux-tower studies, leaving a gap in long-term, spatially continuous, observation-constrained Ω data for the contiguous United States (CONUS). Here, we present a gridded Ω dataset for CONUS from 1982 to 2020 at 0.1° spatial and 8-day temporal resolution. The dataset was generated by combining tower-derived Ω estimates from 74 AmeriFlux sites with gridded meteorological, vegetation, and surface predictors in a specific plant-functional-type (PFT) physics-informed machine learning (PIML) framework. Product reliability was assessed using site-level cross-validation, comparison with a direct machine learning benchmark, feature extrapolation diagnostics, Monte Carlo uncertainty propagation, and pixel-level quality-control flags. The PIML model reproduced tower-derived Ω at withheld sites with a pooled coefficient determination (R^2) of 0.77 and root mean square error (RMSE) of 0.13, and showed clearer gains over direct ML under high extrapolation risk. The gridded product captured expected differences among PFTs, with higher Ω in croplands and lower Ω in open shrublands and savannas, while retaining substantial within-PFT spatial and seasonal variability. Each annual NetCDF file includes three main variables: Ω estimates (‘omega’), associated uncertainty (‘omega_unc’), and quality-control flags (‘QC_flag’). The dataset is available at https://doi.org/10.5281/zenodo.21670853 (Xiong and Feng, 2026).

https://doi.org/10.5194/essd-2026-732
Preprint. Discussion started: 2 November 2026
© Author(s) 2026. CC BY 4.0 License.



Open Access Earth System Science Data Discussions

1 Introduction

Terrestrial evapotranspiration (ET) links the water, energy, and carbon cycles, and plays a central role in land-atmosphere feedbacks and ecosystem functioning (Good et al., 2015; Yang et al., 2023). However, maps of ET magnitude alone do not reveal the coupling regime that governs water exchange between vegetation and the atmosphere. Jarvis and McNaughton (1986) introduced the vegetation–atmosphere decoupling coefficient (Ω) to quantify this regime. Ω values approaching 0 indicate strong coupling to the atmosphere, under which ET is more sensitive to surface conductance (g_s) and atmospheric demand, whereas Ω values approaching 1 indicate increasing decoupling and greater control by available energy. By integrating g_s and aerodynamic conductance (g_a) within the Penman–Monteith (P–M) framework, Ω provides a concise process-based diagnostic of vegetation–atmosphere exchange across biomes (Peng et al., 2019). It has therefore been widely used to diagnose controls on ET and evaluate their representation in land surface models (Li et al., 2026; Zhang et al., 2022; Di et al., 2024), and to inform water resources management (Anderson et al., 2011).

Observational studies have provided important insights into the variability and controls of Ω across ecosystems, but these estimates remain largely limited to flux-tower sites and multisite syntheses (Alves et al., 2022; Zhang et al., 2022). These studies show that Ω varies substantially across seasons, years, and ecosystems in response to canopy development, atmospheric demand, and hydroclimatic conditions. For instance, eddy-covariance (EC) observations have revealed pronounced seasonal and drought-related variations in Ω in individual ecosystems, including Scots pine forests and subtropical mangroves (Zha et al., 2013; Barr et al., 2014). At a broader scale, a synthesis across 21 tropical sites identified systematic differences in Ω along hydroclimatic gradients (Fisher et al., 2009). However, tower-derived Ω estimates are confined to local, temporally varying flux footprints and may not adequately represent the larger, heterogeneous grid cells used in satellite and model products (Chu et al., 2021). Consequently, site observations alone cannot resolve spatial distribution and temporal variability of Ω across climate zones and plant

https://doi.org/10.5194/essd-2026-732
Preprint. Discussion started: 2 November 2026
© Author(s) 2026. CC BY 4.0 License.



functional types (PFTs) over heterogeneous landscapes. Extending these observations to regional scales therefore requires integrating tower-derived Ω estimates with spatially continuous environmental information from remote sensing and reanalysis datasets. Such a gridded product would enable regional diagnosis of how vegetation–atmosphere coupling varies across hydroclimatic conditions and evaluation of its representation in land surface models (LSMs; Novick et al., 2016).

A recent global dataset characterizes land–atmosphere coupling using metrics of soil-moisture control on surface heat fluxes and soil-moisture memory, but it does not quantify the vegetation–atmosphere coupling regime represented by Ω (Tavakoli and Dirmeyer, 2026). Thus, despite recent progress in gridded land–atmosphere diagnostics, no long-term, spatially continuous, tower-constrained Ω product is currently available. Recent advances in machine-learning-based flux upscaling have demonstrated the feasibility of translating eddy-covariance observations into spatially continuous estimates of ecosystem fluxes, such as ET and gross primary production (GPP), by integrating tower measurements with gridded datasets (Jung et al., 2010, 2019; Mu et al., 2013; Beer, 2010; Xiao et al., 2026). However, compared with upscaling ET or GPP, for which the flux estimate itself can serve as the prediction target, constructing a process-based Ω field requires explicit representation of both g_s and g_a, because Ω depends directly on their ratio within the P–M framework. g_s schemes generally require empirical parameterizations of vegetation responses to atmospheric demand and soil-moisture availability, and alternative formulations can produce different g_s and hence Ω estimates, particularly under water-stressed conditions (Han et al., 2023; Bonan et al., 2014; De Kauwe et al., 2015). g_a is likewise sensitive to roughness length and displacement height, which vary with canopy height (Peng et al., 2019), leaf area, and structural heterogeneity but are commonly approximated using static or PFT-level relationships (Maurer et al., 2015). Beyond these parameterization uncertainties, scale mismatches between dynamic EC footprints and gridded environmental datasets can introduce additional uncertainty when transferring tower-derived Ω estimates to regional scales (Chu et al., 2021; Zhang et al., 2022).

https://doi.org/10.5194/essd-2026-732
Preprint. Discussion started: 2 November 2026
© Author(s) 2026. CC BY 4.0 License.



Pure data-driven machine learning (ML) can bypass explicit gridded g_s and g_a parameterization by learning directly from tower-derived Ω, but predictive skill estimated within sampled environmental conditions may not transfer to regions or periods outside the training domain, and unconstrained models do not automatically preserve physical bounds or known process relationships (Reichstein et al., 2019; Shen et al., 2023).

These challenges highlight the need for an upscaling framework that combines physical knowledge with the flexibility of data-driven approaches. Physics-informed ML (PIML) provides such a framework by combining a physically interpretable prior with data-driven correction (Zhao et al., 2019; Eyring et al., 2024). Previous hybrid approaches have incorporated the P–M equation directly within ML architectures to infer physiological or aerodynamic parameters (ElGhawi et al., 2023). In this framework, a prior physical estimate of Ω (Ω_{phys}) is first derived from simplified vegetation–atmosphere exchange theory, and ML models are then trained to estimate the residual between tower-derived Ω observations (Ω_{obs}) and Ω_{phys}. The final estimate is obtained as $\Omega = \Omega_{phys} + \delta_{ML}$ and constrained within the physically meaningful range of 0–1. This design retains an explicit link to conductance theory while allowing machine learning to capture nonlinear, PFT-specific deviations arising from parameter uncertainty, environmental variability, and scale mismatch.

Here, we present an observation-constrained gridded dataset of Ω across the contiguous United States (CONUS) during 1982–2020 at 0.1° spatial resolution and 8-day temporal resolution. CONUS provides a suitable domain for developing and evaluating such a product because it spans broad hydroclimatic gradients and diverse PFTs and is supported by a comparatively dense network of long-term AmeriFlux observations. This combination allows PFT-specific relationships to be developed across diverse environmental conditions and their transfer to previously unseen locations to be evaluated through cross validation. Using tower-derived Ω estimates from 74 AmeriFlux sites representing 8 major PFTs, we combined these observations with geospatial predictors from remote sensing, reanalysis, and ancillary land surface datasets within the PFT-specific PIML upscaling framework. In addition to the primary Ω estimates, we provide Monte

https://doi.org/10.5194/essd-2026-732
Preprint. Discussion started: 2 November 2026
© Author(s) 2026. CC BY 4.0 License.

Open Access Earth System Science Data Discussions

Carlo-propagated input-uncertainty estimates and pixel-level quality-control (QC) information and supporting metadata to facilitate transparent downstream use. We describe the derivation and gridded implementation of Ω, evaluate out-of-site predictive performance and feature-space transfer, quantify propagated input uncertainty and product completeness, and characterize the product's spatial, seasonal, and interannual behavior to guide ecohydrological applications and the evaluation of land surface models.

2 Data sources

2.1 Eddy-covariance data and site selection

AmeriFlux is a network of eddy-covariance sites providing half-hourly or hourly observations of ecosystem carbon, water, and energy fluxes across the Americas (Chu et al., 2023). Using this observation network, we selected eight PFTs: croplands (CRO), grasslands (GRA), evergreen needleleaf forests (ENF), deciduous broadleaf forests (DBF), open shrublands (OSH), mixed forests (MF), savannas (SAV), and woody savannas (WSA). Based on the MODIS MCD12Q1 IGBP land-cover classification, these eight PFTs together accounted for more than 95% of the vegetated within CONUS. To balance temporal coverage against site availability, we applied two sets of initial screening criteria. For the five more extensively sampled PFTs (CRO, GRA, ENF, DBF, and OSH), each represented by at least 10 candidate sites, individual sites were required to be located within CONUS and to have a nominal observational record of at least 10 years. For the three less extensively sampled PFTs (MF, SAV, and WSA), we required at least three candidate sites per PFT and a nominal observational record of at least 5 years per site. Other PFTs were excluded because of their limited areal coverage within the study domain and insufficient numbers of sites meeting the record-length requirements. This initial screening identified 78 candidate sites.

The 78 candidate sites were then screened for the availability and quality of the variables required to derive tower-based Ω, calculate the physical prior, and train the ML models. US-SP2, US-SP3, US-Var, and US-Syv were excluded because extensive data gaps resulted in insufficient valid

https://doi.org/10.5194/essd-2026-732
Preprint. Discussion started: 2 November 2026
© Author(s) 2026. CC BY 4.0 License.

Open Access Earth System Science Data Discussions

samples after quality control and 8-day aggregation. Consequently, 74 sites were retained for the subsequent derivation of tower-based Ω, model training, and independent evaluation (Fig. S1, Table S1).

2.2 Evapotranspiration products and derivation of latent heat flux

To provide the upscaling models with information on realized land-surface water and energy exchange, we included gridded latent heat flux (LE) as a predictor. Because ET estimates differ among products, we used two long-term gridded datasets covering 1982–2020, GLEAM 4.3a at 0.1° daily resolution (Miralles et al., 2025) and GLASS-AVHRR v5.0 at 0.05° and 8-day resolution (Yao et al., 2026) to reduce dependence on any single product. ET from each product was converted to mean LE (W m^{-2}) using the latent heat of vaporization (λ) and its native temporal unit. The two LE estimates were averaged at each grid cell, with the available estimate retained when one product was missing.

2.3 Land cover type, LAI and canopy height

Annual land-cover type was obtained from the ESA Climate Change Initiative and Copernicus Climate Change Service land-cover series (version 2.1.1; Copernicus Climate Change Service, 2019). It provides annual global land-cover classification at a spatial resolution of 300 m. The original 300 m land-cover classes were reclassified into the eight PFTs used in this study according to the crosswalk in Table S2 and were subsequently aggregated to the 0.1° product grid by assigning the modal PFT within each grid cell. Each 0.1° grid cell was assigned the PFT occupying the largest fraction of the underlying 300-m land-cover pixels. No minimum dominant-PFT fraction threshold was imposed. Because temporally consistent land-cover data were unavailable before 1992, the 1992 map was assigned to 1982–1991, thereby assuming unchanged land cover during this pre-1992 interval.

Leaf area index (LAI) was obtained from GIMMS LAI4g V1.2 (Cao et al., 2023). This product provides half-monthly LAI at 1/12° resolution from 1982 to 2020. Its quality flags, fill values, and

https://doi.org/10.5194/essd-2026-732
Preprint. Discussion started: 2 November 2026
© Author(s) 2026. CC BY 4.0 License.



scale factor were applied before spatial and temporal harmonization.

Forest canopy height was obtained from the global forest canopy height dataset of Potapov et al. (2021). Annual forest canopy height for 1982–2020 was reconstructed by combining the canopy-height data with forest-age information from the GAMI v2 Forest Age Dataset (Besnard et al., 2024). For each 0.1° forest grid cell, an empirical relationship between forest age and canopy height was constructed from the corresponding high-resolution subpixels and was used to reconstruct annual canopy height (Fig. S2). Reconstructed forest height was used to parameterize aerodynamic conductance in the estimate of Ω. For short vegetation, prescribed default canopy height values were used instead.

2.4 Meteorological forcing, land-surface variables, and atmospheric CO_2

Meteorological and land-surface variables other than LAI and LE were obtained from ERA5-Land, which provides daily fields on a regular 0.1° grid (Hersbach et al., 2020). We extracted surface downward shortwave radiation (R_g), 2-m air temperature (T_a), 2-m dewpoint temperature (T_{dew}), 10-m u and v wind (WS), total precipitation (Pr), and soil water content (SWC) in soil layer 1 (0−7 cm). No vertical transformation of 10-m u to a canopy-relative reference height was applied in the baseline calculation. After unit conversion, these variables were aggregated to the common 8-day interval and were used as gridded predictors to the estimate of Ω. Horizontal WS was calculated from the native wind components as $\sqrt{u^2+v^2}$ before temporal aggregation. Vapor pressure deficit (VPD) was calculated from T_a and T_{dew}.

Daily atmospheric CO_2 dry-air mole fractions were obtained from the Mauna Loa record maintained by the NOAA Global Monitoring Laboratory (Pétron et al., 2026) and were expressed in parts per million (ppm). Missing daily values were linearly interpolated, and the resulting series was then averaged within each 8-day period. Because the record was used to represent background CO_2, the same 8-day value was assigned to all CONUS grid cells.

https://doi.org/10.5194/essd-2026-732
Preprint. Discussion started: 2 November 2026
© Author(s) 2026. CC BY 4.0 License.

Open Access Earth System Science Data Discussions

2.5 Gridded predictor preprocessing

All gridded inputs (Table S3) were aligned to a common 0.1° regular latitude–longitude grid covering CONUS. Continuous meteorological and satellite fields were resampled by bilinear interpolation. High-resolution vegetation-structure data were aggregated by spatial averaging, whereas annual land cover was aggregated by the modal class. Product-specific quality flags, scale factors, fill values, units, and physically implausible values were handled before spatial and temporal harmonization.

Tower-derived Ω estimates and gridded predictors were harmonized to a common 8-day calendar for model training, validation, and CONUS-wide reconstruction. Each calendar year was represented by 46 nominal 8-day periods defined using a consistent day-of-year sequence. The two half-monthly LAI values in each month were first assigned to their source periods and linearly interpolated to daily values; LAI was then averaged within each 8-day prediction period. Other variables were aggregated to the same periods using variable-specific temporal operators, with state and mean-flux variables averaged and precipitation accumulated over each period. Units, scale factors, fill values, and missing-value codes were standardized before model training and gridded prediction. The same daily-date definition was used for tower observations and gridded predictors. The same aggregation windows and time stamps were applied to tower-derived Ω and all gridded predictors to ensure temporal consistency.

3 Methods

We integrated flux-tower observations, site metadata, meteorological and vegetation predictors, and a physically based Ω prior to generate an 8-day, 0.1° CONUS Ω product for 1982−2020. Raw EC records were processed at their native temporal resolution, including nighttime-record exclusion, energy-balance closure correction, and Ω derivation. All targets, physical estimates, predictors, and model outputs were then aggregated into common 8-day windows. A site-level validation framework is then used to compare the direct ML and PIML. After validation, final

https://doi.org/10.5194/essd-2026-732
Preprint. Discussion started: 2 November 2026
© Author(s) 2026. CC BY 4.0 License.



PIML models are trained and applied to gridded predictors to produce Ω estimates, quality-control layers, uncertainty diagnostics, and summary products for spatial, seasonal, and interannual analyses. To ensure consistency between model development and regional reconstruction, the same gridded predictor products, preprocessing procedures, units, and 8-day temporal definitions were used for both site-level model training and CONUS-wide prediction. The detailed workflow is illustrated in Fig. 1.

3.1 Derivation of site-level Ω

We first excluded nighttime records before deriving site-level Ω. Given the energy balance closure problem in EC flux measurements, where the sum of latent heat (LE) and sensible heat (H) does not match the surface net available energy (Feng et al., 2017; Feng et al., 2019), we applied an energy-balance correction to LE following the method outlined by Jiang et al. (2023). The residual energy (ε_{corr}) was defined as the imbalance between net radiation (R_n) and the sum of turbulent and ground heat fluxes (G). This ε_{corr} was then redistributed proportionally to both the LE and H based on their measured ratio. The energy stored in biomass and soil as well as the energy used in photosynthesis were not determined because the energy storage changes are usually small at 8-d timescales and can be, therefore, neglected (Leuning et al., 2012). For handling timestamps where the correction could not be calculated due to missing data, we used the high-quality (fqc = 0 or 1), gap-filled LE flux calculated by the REddyProc tool. For CRO sites, we retained only observations from the crop growing season, defined as periods when GPP exceeded 15% of the annual maximum GPP, thereby excluding post-harvest bare-soil periods that do not represent vegetation–atmosphere coupling of the active crop canopy.

We calculated surface conductance (g_s), aerodynamic conductance (g_a), and Ω_{obs} at half-hourly level, which were then aggregated to daily values. The daily Ωobs estimates were subsequently averaged within fixed 8-day windows aligned with the gridded predictor data. The observed g_s values of each site can be inverted from the P-M equation:

https://doi.org/10.5194/essd-2026-732
Preprint. Discussion started: 2 November 2026
© Author(s) 2026. CC BY 4.0 License.



$$g_s^{\text{obs}} = \frac{\gamma \cdot LE \cdot g_a^{\text{obs}}}{\Delta \cdot (R_n - G) + \rho_a \cdot C_p \cdot g_a^{\text{obs}} \cdot D - LE \cdot (\Delta + \gamma)} \quad (1)$$

Where ρ is air density (kg m^{-3}), C_p is the specific heat capacity of air (J kg^{-1} $°C^{-1}$), γ is the psychrometric constant (kPa $°C^{-1}$), Δ is the slope of the saturation vapor pressure versus air temperature curve (kPa $°C^{-1}$). g_a^{obs} (m s^{-1}) is calculated by the Monteith-Unsworth equation (Monteith and Unsworth, 2013):

$$g_a^{obs} = \left(\frac{u}{u_*^2} + 6.2 \cdot u_*^{-2/3} \right)^{-1} \quad (2)$$

Where u is the horizontal wind speed (m s^{-1}), and u_* is the friction velocity (m s^{-1}).

$$\Omega_{\text{obs}} = \frac{(\Delta + \gamma)}{\left(\Delta + \gamma \left(1 + g_a^{\text{obs}} / g_s^{\text{obs}} \right) \right)} \quad (3)$$

Following Jarvis and McNaughton (1986), the P-M equation can be rewritten as the weighted sum of equilibrium and imposed LE flux:

$$LE = \Omega LE_{eq} + (1 - \Omega) LE_{imp} \quad (4)$$

where,

$$LE_{eq} = \frac{\Delta}{\Delta + \gamma} (R_n - G), \quad LE_{imp} = \frac{\rho C_p VPD g_s}{\gamma} \quad (5)$$

Here, LE_{eq} represents the energy-limited equilibrium component, whereas LE_{imp} represents the component imposed by atmospheric demand and surface conductance. When Ω values approach 1, ET is primarily controlled by the available energy (R_n-G). On the contrary, when values approach 0, ET is mainly controlled by atmospheric demand and g_s, indicating a strong influence of VPD and the vegetation in the control of ET.

https://doi.org/10.5194/essd-2026-732
Preprint. Discussion started: 2 November 2026
© Author(s) 2026. CC BY 4.0 License.



3.2 PFT-specific physics-informed machine learning framework

We then incorporated the site-level Ω into a PIML framework. Ω_{obs} was derived from tower observations, whereas Ω_{phys} was calculated using gridded meteorological, vegetation, and surface-parameter inputs extracted from the corresponding grid cell. Ω_{phys} was first calculated at the daily scale and then averaged over the same 8-day windows used for Ω_{obs}. The learning target was defined as the residual (δ) between Ω_{obs} and Ω_{phys}, allowing the model to preserve the physical dependence of ET on g_s and atmospheric forcing while correcting systematic, PFT-specific deviations from the theoretical estimate. g_a is computed from the logarithmic wind profile (Jarvis, 1976):

$$g_a^{\text{phys}} = \frac{k^2 u_z}{ln\left[\left(z_m - d\right)/z_{om}\right] ln\left[\left(z_h - d\right)/z_{oh}\right]} \tag{6}$$

$$z_m = \max(10, h+10), z_h = \max(2, h+2) \tag{7}$$

where z_m and z_h represent canopy-height-dependent effective reference heights used in the logarithmic geometry. d is the zero-plane displacement height, z_{om} and z_{oh} are the roughness lengths that govern the transfer of momentum and heat, k is the von Kármán constant (0.41), and u_z is the wind speed measured at the height z_m. Here, d, z_{om}, z_{oh} are estimated as $d = 0.67h$, $z_{om} = 0.123h$, $z_{oh} = 0.1z_{om}$, where h is the canopy height (Allen et al., 1998). The effective reference heights in Eq. (7) were introduced to maintain valid logarithmic-profile geometry across vegetation PFTs. Forest canopy height was derived from the global forest canopy height dataset, whereas prescribed canopy heights were used for other non-forest vegetation types. g_s is modeled following Jarvis-Stewart model (Jarvis, 1976; Stewart, 1988) as a function of various environmental factors, written as:

$$g_{s,p}^{phys} = g_{\max,p} LAI_{eff} f\left(R_g\right) f\left(T_a\right) f\left(VPD\right) f\left(\theta\right) \tag{8}$$

where the subscript p denotes PFT; $g_{\max,p}$ is the maximum surface conductance (m s^{-1}), here refer to the MERRA-GMAO parameter set from the MOD16 Algorithm Theoretical Basis Document

https://doi.org/10.5194/essd-2026-732
Preprint. Discussion started: 2 November 2026
© Author(s) 2026. CC BY 4.0 License.



(Mu et al., 2013); the functions $f(i)$ are scaling terms that reduce g max in response to changes in R_g (W m^{-2}), VPD (kPa), T_a (°C) and SWC (θ, %), which was constrained to the interval [0,1] before being combined with g_{max}. LAI_{eff} is the effective LAI, and can be calculated from LAI by the following equation (Bastiaanssen et al., 2012; Mehrez et al., 1992):

$$LAI_{eff} = \frac{LAI}{0.3LAI + 1.2} \quad (9$$

According to previous studies (Dickinson, 1984; Gentine et al., 2007; Jarvis, 1976; Jarvis and McNaughton, 1986; Noilhan and Planton, 1989; Sellers et al., 1986; Stewart, 1988), environmental stress factors $f(R_g)$, $f(T_a)$, $f(D)$, and $f(\theta)$ are given by:

$$f(R_g) = 1 - \exp\left(-\frac{R_g}{k_{R_g}}\right) \quad (10)$$

$$f(T_a) = 1 - \left(\frac{T_a - T_{opt}}{T_{opt}}\right)^2 \quad (11)$$

$$f(VPD_0) = 1 - K_{D_0} * VPD_0 \quad (12)$$

$$f(\theta) = \begin{cases} 0 & ,\theta < \theta_w \\ \dfrac{\theta - \theta_w}{\theta_c - \theta_w} & ,\theta_w < \theta < \theta_c \\ 1 & ,\theta > \theta_c \end{cases} \quad (13)$$

where T_{opt} is the optimal air temperature for plant transpiration depending on vegetation type, here refers to Xia et al. (2026). k_{Rg} and k_{D0} are coefficients and were here set at 500 W m^{-2} and 0.238 (kPa^{-1}), respectively (Cui et al., 2021); θ_c and θ_w are field capacity (cm^3 cm^{-3}) and wilting point (cm^3 cm^{-3}), derived from Gupta et al. (2023).

The physical calculation does not explicitly represent all effects of vegetation structure, parameter variability, input-product bias, and spatial-scale mismatch. We therefore used tower-derived observations to estimate the remaining discrepancy through residual learning. For observation i

https://doi.org/10.5194/essd-2026-732
Preprint. Discussion started: 2 November 2026
© Author(s) 2026. CC BY 4.0 License.



298 belonging to PFT p, the residual target was defined as:

299 $$\delta_{\Omega,i,p} = \Omega_{\mathrm{obs},i,p} - \Omega_{phy,i,p} \quad (14)$$

300 A PFT-specific ML, M_p, was trained to estimate this residual:

301 $$\delta_{\Omega,i,p} = M_p(x_{i,p}) \quad (15)$$

302 Where $x_{i,p}$ represents the predictor vector. The unconstrained corrected estimate was calculated as
303 the sum of the Ω_{phys} and the predicted δ. The final estimate was clipped to the physically admissible
304 range:

305 $$\hat{\Omega}_{i,p} = \min\left[1, \max\left(0, \Omega_{phys,i,p} + \hat{\delta}_{\Omega,i,p}\right)\right] \quad (16)$$

306 The training, validation, and gridded implementation of the PFT-specific residual models are
307 described in *Methods* 3.3.

308 **3.3 Model training, validation, and gridded prediction**

309 Model training was conducted separately for each PFT using the XGBoost algorithm, a gradient-
310 boosting approach widely applied in ecological and environmental modelling (Chen and Guestrin,
311 2016; Lin et al., 2026). XGBoost hyperparameters were fixed across PFTs and were not tuned
312 separately for individual types. Before training, each 8-day sample was paired with gridded
313 meteorological, vegetation, and surface predictors extracted from the corresponding 0.1° grid cell.
314 This tower-to-grid pairing means that the learned residual includes both physical-formulation bias
315 and representativeness differences between EC footprints and 0.1° grid cells. Samples with missing
316 target values or physically implausible predictor values were excluded before training.

317 We trained two model configurations to benchmark the physics-informed formulation against a
318 direct ML approach. Both models used the same base set of gridded environmental predictors (X),
319 tower samples, site-blocked cross-validation splits, and parameterization. Direct ML predicted Ω_{obs}

https://doi.org/10.5194/essd-2026-732
Preprint. Discussion started: 2 November 2026
© Author(s) 2026. CC BY 4.0 License.



directly from X. In contrast, PIML model learned the $\delta = \Omega_{obs} - \Omega_{phys}$ using X together with Ω_{phys} as predictors, and reconstructed the final estimate as $\Omega = \Omega_{phys} + \delta_{ML}$. Thus, the comparison was intended to evaluate the complete PIML formulation relative to Direct ML, rather than to isolate the individual contributions of residual learning and the additional Ω_{phys} predictor. This paired design therefore provides a benchmark of the complete PIML framework against a direct ML formulation under otherwise consistent training and validation conditions.

Model performance was evaluated using site-blocked cross-validation. For each PFT, sites were randomly divided into five folds, with four folds used for training and the remaining fold used for validation. Each flux site was assigned entirely to one fold so that predictions were evaluated at sites excluded from model fitting. For WSA and MF, which were represented by fewer than five sites, the number of folds was set to the maximum feasible number of site groups. Sites located within 0.1° of each other were assigned to the same fold to reduce information leakage between nearby, potentially non-independent observations. Model performance against tower-derived Ω_{obs} was quantified using coefficient of determination (R^2), root mean square error (RMSE), mean absolute error (MAE) and bias based on the pooled out-of-fold predictions.

We further examined model performance in relation to feature-space extrapolation risk. For each PFT and cross-validation split, the well-sampled range of each predictor was defined by the 5th–95th percentile interval of the training samples. A held-out sample was marked as out of range for a predictor if its value fell outside this interval. The extrapolation-risk score was then calculated as the fraction of predictors outside the training range. Low-, medium-, and high-risk cases were defined by tertiles of this score across the cross-validation samples. Because tower observations were not available for the full 1982–2020 reconstruction period, this site-level validation mainly evaluates spatial transfer to unseen sites rather than temporal extrapolation to the early reconstruction period.

After validation, final PFT-specific models were trained using all available tower samples and

https://doi.org/10.5194/essd-2026-732
Preprint. Discussion started: 2 November 2026
© Author(s) 2026. CC BY 4.0 License.



applied to the 8-day, 0.1° gridded predictor fields across CONUS for 1982–2020. The final outputs included gridded Ω estimates, quality-control flags, and uncertainty diagnostics for subsequent spatial, seasonal, and interannual analyses.

3.4 Uncertainty propagation and quality control

Uncertainty in the gridded Ω product was estimated using a Monte Carlo (MC) propagation framework. The procedure was applied to the same 8-day predictor, CONUS vegetation mask, Ω_{phys} calculation, and final δ correction models across PFTs used for the gridded prediction. For each grid cell and 8-day period, meteorological, vegetation, flux-related, and surface-parameter inputs were randomly perturbed according to prescribed uncertainty distributions. The perturbation scheme and one-standard-deviation magnitudes are summarized in Fig. S3a, b.

For each MC realization, Ω_{phys} was recomputed from the perturbed physical variables and parameters. The trained δ model was then applied to the predictor set, and the corrected Ω estimate was calculated using the same prediction workflow as the final product. This step ensured that uncertainty was propagated through both the physical Ω calculation and the ML δ correction. In the released product, the MC ensemble consisted of 100 realizations for each prediction step. The variable Ω_{unc} represents the width of the MC uncertainty interval. It was calculated as the difference between the 95th and 5th percentiles of the ensemble Ω estimates for each grid cell and 8-day period.

Pixel-level quality control was implemented during gridded prediction and stored as the variable 'QC_flag' in the annual NetCDF files. Required predictors were checked before prediction, and pixels with missing or physically implausible input values were flagged. The unconstrained Ω estimates were also checked against the theoretical range of 0–1 before clipping. The released 'QC_flag' variable uses four integer classes: 0 for valid estimates, 1 for missing or invalid predictor information, 2 for estimates outside the physical bounds before clipping, and 4 for pixels outside the target CONUS vegetation domain. This flag layer allows users to apply analysis-specific

https://doi.org/10.5194/essd-2026-732
Preprint. Discussion started: 2 November 2026
© Author(s) 2026. CC BY 4.0 License.

Open Access Earth System Science Data Discussions

screening criteria. For conservative applications, we recommend using only pixels with 'QC_flag' = 0; for applications requiring greater spatial or temporal coverage, flagged pixels can be retained with explicit consideration of their diagnostic meaning.

4 Results

4.1 Site observations and representativeness

The 74 EC sites covered 8 PFTs across CONUS, but their distribution was uneven (Fig. 2a and Table S1). GRA (n = 16) and CRO (n = 13) had the largest number of sites, whereas MF and WSA were represented by only 3 and 4 sites, respectively. The network extended across western, central, and eastern CONUS, although several areas contained few or no sites (Fig. S1). At tower-level, observed Ω differed strongly among sites and vegetation types. Site-mean values ranged from 0.05 to 0.86, with a median of 0.30. CRO had the highest PFT mean (0.64 ± 0.12), while OSH and WSA had the lowest means (0.13 ± 0.05 and 0.14 ± 0.03, respectively; Fig. 2a). DBF and GRA had similar PFT means, but GRA showed a much wider spread among sites. Clear within-PFT differences were also present for ENF and CRO (Fig. S4). The substantial within-PFT variability suggests that environmental conditions beyond vegetation classification are required to explain spatial variations in Ω. Thus, PFT categories were associated with broad contrasts in observed Ω, while substantial within-PFT variability remained.

The available tower observations did not indicate a consistent directional change across the sampled sites (Fig. 2b). Positive and negative trends, quantified using Sen's slope estimator and tested using the Mann–Kendall test, occurred at 37 and 37 sites, respectively, and the median slope was close to 0. Only 15 sites had significant trends ($p < 0.05$), including 7 positive and 8 negative trends. Most were found in ENF, DBF, and GRA, while no significant trend was detected for OSH, SAV, or WSA. However, the number of sites differed among PFTs, so these counts are not directly comparable and do not indicate differences in trend prevalence among PFTs. Opposite trends also occurred within the same PFT. The observed changes were therefore local rather than a consistent

https://doi.org/10.5194/essd-2026-732
Preprint. Discussion started: 2 November 2026
© Author(s) 2026. CC BY 4.0 License.

Open Access Earth System Science Data Discussions

shift across CONUS.

4.2 Site-independent validation and extrapolation robustness

The site-level test showed that PIML captured much of the 8-day variation in Ω at sites excluded from model training. Pre-clipping boundary violations were uncommon for both models. Among out-of-fold predictions, 0.90% of pooled PIML out-of-fold predictions and 1.15% of Direct ML predictions fell outside the physical range of [0,1]. Across the 74 sites, the pooled R^2 was 0.77 and the RMSE was 0.13. Predictive performance was positive for all PFTs (Fig. S5), with variation among vegetation types: R^2 exceeded 0.75 for ENF, OSH, and GRA, whereas lower values were found for DBF and WSA (Fig. 3b). The lower performance for some PFTs may partly reflect limited observational constraints, particularly for sparsely sampled ecosystems such as WSA and MF. Sites with longer records generally had higher skill (Spearman's $\rho = 0.56$), while skill tended to decline as the observed mean Ω increased ($\rho = -0.40$; Fig. 3c).

PIML and Direct ML had similar performance under the test (Fig. S6). Direct ML gave a slightly higher pooled R^2 than PIML (0.79 and 0.77, respectively), with a small difference in RMSE (0.12 and 0.13). Both data-driven models substantially outperformed the simplified physical baseline, for which R^2 was 0.34. The relative performance of the two data-driven models varied among PFTs. PIML performed better for ENF and MF, while the largest loss relative to Direct ML occurred for WSA. However, the relative advantage of PIML became more apparent as feature-space extrapolation risk increased (Fig. 4). Their performance was close in the low-risk class, where the mean difference in R^2 was 0.015 ± 0.004. The difference increased to 0.17 ± 0.04 in the high-risk tertile (extrapolation risk > 0.15). Median risk was higher for MF, GRA, and SAV, although the response varied among individual model runs (Fig. 4a–c). These PFTs generally have fewer flux sites or broader environmental distributions, increasing the likelihood that gridded predictors fall outside the conditions sampled by tower observations, with CO_2, LAI, LE, and SWC being the main sources of risk (Fig. 4d).

https://doi.org/10.5194/essd-2026-732
Preprint. Discussion started: 2 November 2026
© Author(s) 2026. CC BY 4.0 License.



The leading predictors also differed among PFTs (Fig. 3d). LE had the largest contribution for five of the 8 PFTs. Because Ω is derived from ecosystem water and energy exchange, this ranking represents predictive contribution within the model rather than an independent causal effect. Precipitation was most important for ENF, while DOY and R_g ranked first for WSA and SAV, respectively. The physical information (Ω_{phys}) remained among the five leading predictors for DBF, OSH, SAV, and GRA. Predictor importance was therefore PFT-specific rather than common across vegetation types. As an additional product-consistency check, we further evaluated whether the reconstructed gridded Ω product reproduced tower-derived site characteristics. At the product scale, gridded and observed site means were correlated (R = 0.79; Fig. S7a), but the gridded values were lower on average (bias = −0.08; Fig. S7b). The negative bias was strongest for CRO and DBF. Site-level trend agreement was more sensitive to record length: when all sites with at least five paired years were included, annual trends showed weak agreement, whereas restricting the comparison to long-record sites with at least 15 paired years improved the trend correlation (R = 0.66, Fig. S7c, d).

4.3 Spatiotemporal patterns of the gridded Ω product

The gridded product resolved clear spatial variation in long-term mean Ω across CONUS (Fig. 5a). Higher values occurred across the central cropland belt, the northern Great Plains, and parts of the eastern CONUS. Lower values were more common across the arid and mountainous West. The PFT means also differed. CRO had the highest mean Ω (0.53 ± 0.04, here only spatial SD). OSH and SAV had the lowest means (0.23 ± 0.08 and 0.24 ± 0.04, respectively). Considerable spatial variation remained within each PFT. The product therefore retained spatial information beyond the categorical PFT map. The main PFT differences remained through the 1982−2020 record (Fig. 5b, Figs. S8, S9). CRO stayed highest in all years, and WSA, DBF, ENF, MF, and GRA occupied a narrower middle range, while OSH and SAV were lower. Annual mean Ω changed little for most PFTs, but the long-term trends differed among groups (Fig. 5c, d). SAV increased by 0.006 decade^{-1} ($p < 0.01$), and ENF increased by 0.0014 decade^{-1} ($p < 0.001$). WSA decreased by 0.004 decade^{-1}

https://doi.org/10.5194/essd-2026-732
Preprint. Discussion started: 2 November 2026
© Author(s) 2026. CC BY 4.0 License.

Open Access Earth System Science Data Discussions

($p < 0.001$). Trends in DBF, MF, OSH, GRA, and CRO were small and not significant. Pixel-level trends were more mixed than the PFT means, with positive values in 58% of valid grid cells and negative values in 42%. Areas of increase and decrease occurred within the same PFTs, especially across the western and central CONUS. Thus, the product represented local trend differences that were not apparent from PFT-level averages alone.

Seasonal range varied across CONUS, with a median of 0.21 across valid grid cells (Fig. 6a). Larger ranges occurred in the western mountains, Great Plains, and cropland regions, whereas smaller ranges occurred in the Southwest and eastern forests. PFT seasonal cycles differed in magnitude and timing (Fig. 6b and c). CRO remained highest, SAV had the largest range with a mid-year maximum, WSA peaked early, and OSH and GRA peaked late. Seasonal trends also differed among PFTs (Fig. 6d). SAV increased and WSA decreased during most periods, while the other PFTs showed mixed or season-specific trends. Together, these results show that the product resolves spatial, annual, and seasonal variations in Ω rather than representing only long-term PFT means.

4.4 Product uncertainty, completeness, and quality-control diagnostics

The Monte Carlo (MC) represents uncertainty associated with the sampled inputs and parameters rather than total product uncertainty (Fig. S3c). The DBF and GRA examples had compact Ω distributions, whereas the CRO showed greater sensitivity to perturbations due to human interference possibly. The convergence test showed that the uncertainty estimate stabilized as the number of realizations increased (Fig. S3d). The median and mean ratios of uncertainty to the 100-realization estimate approached 1.0 by about 40 realizations. The interquartile range across pixels also narrowed as the number of realizations increased.

At the product scale, missing rate and MC uncertainty showed different spatial patterns (Fig. 7a and b). Most target grid cells had no missing 8-day estimates over 1982−2020. The median and 95th percentile of the missing rate were both 0, although local maxima reached 1.0 in small western

https://doi.org/10.5194/essd-2026-732
Preprint. Discussion started: 2 November 2026
© Author(s) 2026. CC BY 4.0 License.



patches. MC uncertainty was more spatially continuous. Its median was 0.15, with 90% of grid-cell means between 0.09 and 0.18. The correlation between missing rate and MC uncertainty was weak (r = −0.02). Across the 8-day spatial means from 1982 to 2020, uncertainty was lowest for MF (0.08 ± 0.01, Fig. S10) and highest for CRO (0.17 ± 0.01) and DBF (0.16 ± 0.02). Mean uncertainty was 0.12 ± 0.02 for GRA, 0.13 ± 0.01 for OSH, 0.14 ± 0.02 for ENF and WSA, and 0.14 ± 0.04 for SAV. Seasonal changes were larger than interannual variation, while annual PFT means showed no common long-term change.

To retain information on physically implausible predictions masked by the final [0,1] constraint, we quantified the pre-clipping outside rate (Fig. 7c). The Low issue class accounted for 95.4% of the target domain, while High missing and Clipped issue cells accounted for 3.2% and 1.5%, respectively. Product completeness was highest for ENF (98.3%), followed by SAV and GRA (97.3% and 97.2%, Fig. 7d), and WSA had the lowest value (84.0%). These contrasts were mostly stable through the record (Fig. S11). WSA was the main exception, increasing from 0.72 in 1982 to 0.94 in 2020, due to changes in the pixels classified as WSA in the annual land-cover data. Across the full domain, the annual low-issue fraction averaged 95.7% and ranged from 94.9% to 96.4%. Sensitivity to very low-LAI periods was small (Fig. S12). Masking periods with missing LAI or LAI ≤ 0.1 (Lian et al., 2022) removed 1.6% of otherwise valid estimates. The mean change in the CONUS annual mean Ω was −0.001. The largest absolute change in the CONUS annual mean was 0.004. The largest absolute PFT-year change was 0.009 and occurred for GRA in 2010. The CONUS trend changed by −0.0003 decade^{-1}, and the signs of all PFT trends remained unchanged.

5 Discussion

5.1 Reducing uncertainties in Ω upscaling

Upscaling Ω differs from GPP or ET. Ω is a derived diagnostic, so uncertainty can enter through the EC towers, gridded predictors, physical conductance assumptions, and model transfer. Similar uncertainty pathways have been discussed for FLUXCOM, CEDAR-GPP, ET fusion products, and

https://doi.org/10.5194/essd-2026-732
Preprint. Discussion started: 2 November 2026
© Author(s) 2026. CC BY 4.0 License.


process-based flux datasets (Tramontana et al., 2016; Jung et al., 2019; Leng et al., 2024; Kang et al., 2025; Wu et al., 2025), but here they are separated into components that are quantified, diagnosed, or left as limitations (Table 1).

The first source of uncertainty is the EC-derived Ω target. EC observations are affected by measurement error, data gaps, filtering choices, and energy-balance closure (Baldocchi, 2008; Papale et al., 2006; Pastorello et al., 2020). Physical-range screening, energy-balance checks, and 8-day aggregation reduced random noise and removed unrealistic values, but they cannot remove systematic EC errors. For example, different energy-balance correction assumptions may also affect LE and H differently (Stoy et al., 2013; Jung et al., 2019). Tower representativeness is likely a larger limit. Flux towers are unevenly distributed across climate space, vegetation types, and terrain (Tramontana et al., 2016; Jung et al., 2019). WSA illustrates this limitation: despite reasonable agreement between tower and matched-grid means (Fig. S7b), its all-grid mean is less certain because it includes conditions poorly represented by the available towers. However, it accounts for only ~0.1% of the mapped vegetated area. Estimates for sparsely sampled PFTs, particularly MF and WSA, should be therefore interpreted together with the site-level validation and extrapolation diagnostics.

The second uncertainty source is the set of gridded predictors. Remote sensing and reanalysis products contain retrieval error, missing data, scale mismatch, and temporal changes in data quality. For example, LAI products still differ because of retrieval algorithms, angular effects, cloud and aerosol screening, background soil effects, sensor degradation in long-term records and validation limits (Fang et al., 2019). Soil moisture and meteorological forcing add further uncertainty, especially in drylands and transition zones where water supply and atmospheric demand both matter (Dirmeyer, 2011; Novick et al., 2016; Quets et al., 2019; Chen et al., 2019). The choice of controlling factors also affects the product. Because canopy height, roughness, leaf area, root access, and maximum conductance vary strongly across forests, grasslands, shrublands, and crops (Grossiord et al., 2020). PFTs group vegetation into broad classes, but locations within the same

https://doi.org/10.5194/essd-2026-732
Preprint. Discussion started: 2 November 2026
© Author(s) 2026. CC BY 4.0 License.

Open Access Earth System Science Data Discussions

PFT still differ in canopy structure and environmental conditions. The spatial variation in Ω within each PFT therefore contains information beyond land-cover type and cannot be represented by PFT means alone.

Scale mismatch is closely linked to predictor uncertainty. The product grid is coarser than many EC footprints, and the gridded predictors may smooth local variation in vegetation, soil, and terrain. Similar scale issues have been discussed for flux-tower representativeness and satellite validation (Chu et al., 2021). Land-cover and PFT assignment can also affect PFT means and valid fractions, especially where mixed land covers are common. Recent ET data products have treated land-cover stability and forcing consistency as key robustness checks (Feng et al., 2025; Wu et al., 2025). In the present product, PFT-consistent matching and checks for invalid predictor values reduced some scale mismatch, but PFT means should still be interpreted with the QC flags and extrapolation diagnostics. Temporal consistency is another source of uncertainty for the 1982–2020 reconstruction. The model was trained mainly with EC observations from recent decades, but it was applied across a longer period. Long records depend on stable relationships among predictors, canopy function, and Ω. They also depend on consistent input data across sensor eras and reanalysis periods. CEDAR-GPP and P-LSHv2 both highlight this issue for long-term GPP and ET products (Kang et al., 2025; Feng et al., 2025). A further limitation applies to 1982–1991, for which the 1992 land-cover map was used because temporally consistent annual land-cover information was unavailable. This assumption may introduce local uncertainty in areas that experienced substantial land-cover change before 1992, and early-period PFT-specific estimates should therefore be interpreted with additional caution. The annual QC analysis and low-LAI sensitivity test provide useful checks, but they cannot prove that all early-period or local trends are free from input-driven artifacts.

The final uncertainty source is model transfer. PIML showed a larger improvement over Direct ML in high-risk cases than in low-risk cases. Furthermore, feature-space diagnostics indicated where the remaining risk arose. The main out-of-range predictors differed among PFTs, and CO_2, LAI,

https://doi.org/10.5194/essd-2026-732
Preprint. Discussion started: 2 November 2026
© Author(s) 2026. CC BY 4.0 License.

Open Access Earth System Science Data Discussions

548 LE, and SWC were frequent sources of risk. This pattern shows why extrapolation should be
549 assessed in predictor space rather than by geographic distance alone (Booker and Whitehead, 2018).
550 It also suggests that future versions would benefit from more EC sites in weakly sampled PFTs,
551 improved vegetation structure and soil-water inputs, and predictor ensembles that represent
552 alternative source products. Uncertainty quantification remains difficult for upscaling products.
553 Cross-validation mainly estimates predictive error within the sampled domain, whereas MC spread
554 represents only the uncertainty sources included in the perturbation design (Jung et al., 2019;
555 Haynes et al., 2023; Kang et al., 2025), not as a total error bound. It does not account for all
556 uncertainties in tower-derived Ω, model structure, or extrapolation beyond the sampled predictor
557 space.

558 In summary, the current uncertainty treatment is most useful for comparing relative reliability
559 across space, PFTs, and seasons. It is less suited for assigning a full probabilistic error bound to
560 each Ω estimate. More complete uncertainty quantification would require additional EC sites,
561 perturbation of more source products, site-bootstrap ensembles, independent evaluation data, and
562 tests of structural assumptions in the Ω_{phys}.

563 **5.2 Product strengths and user guidance**

564 The main contribution of this product is the extension of a tower-based coupling diagnostic to a
565 gridded 0.1° record for CONUS. Eddy-covariance observations allow Ω to be estimated at
566 individual sites, but they do not provide continuous spatial regional coverage. Existing tower-
567 upscaling products mainly describe carbon, water, and energy fluxes (Tramontana et al., 2016; Jung
568 et al., 2019). The Ω product complements these datasets by describing the coupling regime under
569 which vegetation–atmosphere exchange occurs, rather than providing another estimate of flux
570 magnitude. The temporal coverage is another strength. The 1982–2020 record allows analysis of
571 seasonal cycles, interannual variability, and long-term changes under rising CO_2, warming, and
572 increasing atmospheric demand. The 8-day temporal resolution is suited to seasonal and event-

https://doi.org/10.5194/essd-2026-732
Preprint. Discussion started: 2 November 2026
© Author(s) 2026. CC BY 4.0 License.

Open Access Earth System Science Data Discussions

scale studies. It is not as fine as hourly EC data, but it is closer to vegetation and hydrometeorological dynamics than annual products. Other products with high temporal resolution have shown value for studying diurnal, daily, or event-scale ecosystem and hydrological responses (Leng et al., 2024; Huang et al., 2024).

Ω has a clear process meaning, which represents the relative weighting of equilibrium evaporation and imposed evaporation, and therefore the sensitivity of ET to surface and atmospheric control (Jarvis and McNaughton, 1986; McNaughton and Jarvis, 1991; Knauer et al., 2018). Low Ω ($g_a \rightarrow \infty$) indicates stronger coupling and greater sensitivity to g_s. High Ω ($g_s \rightarrow \infty$) indicates greater decoupling and a stronger influence of available energy. Site-based studies have shown marked differences among vegetation types and have proposed Ω as a benchmark for canopy coupling (De Kauwe et al., 2017). The gridded record allows these differences to be compared across PFTs, regions, seasons, decades using one consistent metric.

LSMs evaluation is one of the clearest uses of the product. First, site-scale comparisons have shown substantial differences in the magnitude of Ω derived from EC observations, LSMs, and reanalysis datasets, with the size of these differences varying among PFTs (Peng et al., 2019; Zhang et al., 2022). This gridded product can extend these comparisons from individual sites to regional spatial patterns and seasonal amplitude and timing. In addition, when combined with modeled transpiration (T), soil evaporation, interception, g_s and g_a, VPD, SWC and LAI, the magnitude and seasonal amplitude of Ω provide a process-level test (Medlyn et al., 2011; Novick et al., 2016; Zhang et al., 2022). For example, the Ω value obtained from tower observations is to some extent proportional to T/ET, while models yield the opposite conclusion because they do not consider soil evaporation from vegetated areas (Peng et al., 2019). This contrast indicates that ET partitioning can contribute to disagreement in model-derived Ω. Comparing the modeled Ω–T/ET relationship with the EC-derived relationship can help determine whether ET partitioning is a likely source of that disagreement.

https://doi.org/10.5194/essd-2026-732
Preprint. Discussion started: 2 November 2026
© Author(s) 2026. CC BY 4.0 License.


The product can also support analyses of hydroclimatic variation in coupling. Atmospheric demand and soil moisture exert distinct controls on stomatal behavior and ecosystem fluxes (Novick et al., 2016; Grossiord et al., 2020; Kannenberg et al., 2024). Ω anomalies can be compared across drought and wet periods, or within the same PFT across climate zones, to test whether coupling responds differently under contrasting water availability. These patterns can also serve as evaluation targets for models that use fixed parameters within a PFT.

The released Ω estimates should be screened with the accompanying MC uncertainty, QC flags, annual PFT maps, and valid-fraction information. Ω_{unc} represents the spread propagated from the perturbations included in the MC design and is not a total error bound. The QC flags identify missing estimates and pre-clipping range violations, while the valid fraction summarizes temporal completeness. Comparisons are therefore more robust for spatial, seasonal, or PFT contrasts than for assigning an exact Ω value to one grid cell.

5. Conclusion

We developed a long-term, observation-constrained Ω dataset for CONUS from 1982 to 2020 at 0.1° spatial resolution and 8-day temporal resolution. The product links tower-derived Ω estimates with gridded meteorological, vegetation, and surface predictors through a PFT-specific PIML framework. By correcting a physically based Ω prior with tower-observed residuals, the dataset keeps a direct connection to vegetation-atmosphere exchange theory while allowing systematic, PFT-specific departures from the simplified physical calculation.

The validation and diagnostic analyses show that the product captures much of the observed site-level variation in Ω. The validation gave a pooled R^2 of 0.77 and RMSE of 0.13, and the physics-informed model gave clearer benefits under high feature-space extrapolation risk. The gridded product also showed coherent spatial and seasonal patterns across CONUS, with higher Ω in cropland-dominated regions and lower Ω in more strongly coupled dryland and shrubland regions. These patterns indicate that the dataset contains information beyond static land-cover classes and

https://doi.org/10.5194/essd-2026-732
Preprint. Discussion started: 2 November 2026
© Author(s) 2026. CC BY 4.0 License.



623 can support regional analysis of vegetation-atmosphere coupling.

624 The released dataset includes Ω estimates, MC uncertainty, and pixel-level QC flags. These layers
625 allow users to screen the product according to their own tolerance for missing data, clipping, and
626 propagated uncertainty. The uncertainty estimate does not include all possible errors, especially
627 tower representativeness error, structural model uncertainty, and all source-product biases. With
628 these limits in mind, the dataset provides a new benchmark for studying hydroclimatic variation in
629 vegetation-atmosphere coupling and for evaluating land surface models.

630 **Data availability**

631 The gridded vegetation–atmosphere decoupling coefficient dataset described in this paper is freely
632 available at https://doi.org/10.5281/zenodo.21670853 (Xiong and Feng, 2026). The dataset covers
633 the contiguous United States from 1982 to 2020 at 0.1° spatial and 8-day temporal resolution. It is
634 provided as annual NetCDF files containing Ω estimates, Monte Carlo-propagated input
635 uncertainty (Ω_{unc}), and the pixel-level quality-control variable (QC_flag). The dataset is released
636 under the Creative Commons Attribution 4.0 International (CC BY 4.0) licence.

637 **Acknowledgments**

638 This work was supported by the National Natural Science Foundation of China (Grant No.
639 42571123), the funding agencies of Zhejiang Province and Ningbo Municipality through the
640 program “Novel Technologies for Joint Pollution Reduction and Carbon Sequestration”, and
641 Ningbo Natural Science Foundation (Grant No. 2025J026).

642 This study relied on valuable data provided by AmeriFlux. Funding for the AmeriFlux data service
643 was provided by the U.S. Department of Energy Office of Science. We thank the significant and
644 tireless efforts of the AmeriFlux PIs, their teams, and the funding agencies. We are deeply grateful
645 for their hard work in maintaining these invaluable long-term datasets and making them openly
646 available for analysis.

https://doi.org/10.5194/essd-2026-732
Preprint. Discussion started: 2 November 2026
© Author(s) 2026. CC BY 4.0 License.



Open Access Earth System Science Data Discussions

Conflict of Interest Statement

The authors declare there are no conflicts of interest for this manuscript.

https://doi.org/10.5194/essd-2026-732
Preprint. Discussion started: 2 November 2026
© Author(s) 2026. CC BY 4.0 License.



References

Allen, R. G., Pereira, L. S., Raes, D., and Smith, M.: Crop evapotranspiration-Guidelines for computing crop water requirements-FAO Irrigation and drainage paper 56, Fao, Rome, 300, D05109, https://www.fao.org/4/x0490e/x0490e00.htm, 1998.

Alves, J. D. N., Ribeiro, A., Rody, Y. P., and Loos, R. A.: Energy balance and surface decoupling factor of a pasture in the Brazilian Cerrado, Agric. For. Meteorol., 319, 108912, https://doi.org/10.1016/j.agrformet.2022.108912, 2022.

Anderson, M. C., Hain, C., Wardlow, B., Pimstein, A., Mecikalski, J. R., and Kustas, W. P.: Evaluation of Drought Indices Based on Thermal Remote Sensing of Evapotranspiration over the Continental United States, J. Clim., 24, 2025-2044, https://doi.org/10.1175/2010JCLI3812.1, 2011.

Baldocchi, D.: 'Breathing' of the terrestrial biosphere: lessons learned from a global network of carbon dioxide flux measurement systems, Aust. J. Bot., 56, 1-26, https://doi.org/10.1071/BT07151, 2008.

Barr, J. G., DeLonge, M. S., and Fuentes, J. D.: Seasonal evapotranspiration patterns in mangrove forests, J. Geophys. Res.: Atmos., 119, 3886-3899, https://doi.org/10.1002/2013JD021083, 2014.

Bastiaanssen, W. G. M., Cheema, M. J. M., Immerzeel, W. W., Miltenburg, I. J., and Pelgrum, H.: Surface energy balance and actual evapotranspiration of the transboundary Indus Basin estimated from satellite measurements and the ETLook model, Water Resour. Res., 48, https://doi.org/10.1029/2011WR010482, 2012.

Beer, C., Reichstein, M., Tomelleri, E., Ciais, P., Jung, M., Carvalhais, N., Rödenbeck, C., Arain, M. A., Baldocchi, D., Bonan, G. B., Bondeau, A., Cescatti, A., Lasslop, G., Lindroth, A., Lomas, M., Luyssaert, S., Margolis, H., Oleson, K. W., Roupsard, O., Veenendaal, E., Viovy, N., Williams, C., Woodward, F. I., and Papale, D.: Terrestrial gross carbon dioxide uptake: Global distribution and covariation with climate, Science, 329, 834-838,

https://doi.org/10.5194/essd-2026-732
Preprint. Discussion started: 2 November 2026
© Author(s) 2026. CC BY 4.0 License.



https://doi.org/10.1126/science.1184984, 2010.

Besnard, S. S., Maurizio; Herold, Martin; Cartus, Oliver; Gütter, Jonas; Heinrich, Viola H.A.; Herault, Bruno; Kassi, Justin; Koirala, Sujan; N'Guessan, Anny; Neigh, Christopher; Nelson, Jacob A.; Poulter, Benjamin; Weber, Ulrich; Zhang, Tao; Carvalhais, Nuno: Global Age Mapping Integration (GAMI). V. 2.1, GFZ Data Services, https://doi.org/10.5880/GFZ.1.4.2023.006, 2024.

Bonan, G. B., Williams, M., Fisher, R. A., and Oleson, K. W.: Modeling stomatal conductance in the earth system: linking leaf water-use efficiency and water transport along the soil–plant–atmosphere continuum, Geosci. Model Dev., 7, 2193-2222, http://doi.org/10.5194/gmd-7-2193-2014, 2014.

Booker, D. J. and Whitehead, A. L.: Inside or Outside: Quantifying Extrapolation Across River Networks, Water Resour. Res., 54, 6983-7003, https://doi.org/10.1029/2018WR023378, 2018.

Cao, S., Li, M., Zhu, Z., Wang, Z., Zha, J., Zhao, W., Duanmu, Z., Chen, J., Zheng, Y., Chen, Y., Myneni, R. B., and Piao, S.: Spatiotemporally consistent global dataset of the GIMMS leaf area index (GIMMS LAI4g) from 1982 to 2020, Earth Syst. Sci. Data, 15, 4877-4899, http://doi.org/10.5194/essd-15-4877-2023, 2023.

Chen, F., Crow, W. T., Cosh, M. H., Colliander, A., Asanuma, J., Berg, A., Bosch, D. D., Caldwell, T. G., Collins, C. H., and Jensen, K. H.: Uncertainty of reference pixel soil moisture averages sampled at SMAP core validation sites, J. Hydrometeorol., 20, 1553-1569, 2019.

Chen, T. and Guestrin, C.: Xgboost: A scalable tree boosting system, Proceedings of the 22nd acm sigkdd international conference on knowledge discovery and data mining, 785-794, https://doi.org/10.1145/2939672.2939785, 2016.

Chu, H., Christianson, D. S., Cheah, Y.-W., Pastorello, G., O'Brien, F., Geden, J., Ngo, S.-T., Hollowgrass, R., Leibowitz, K., Beekwilder, N. F., Sandesh, M., Dengel, S., Chan, S. W., Santos, A., Delwiche, K., Yi, K., Buechner, C., Baldocchi, D., Papale, D., Keenan, T. F., Biraud, S. C., Agarwal, D. A., and Torn, M. S.: AmeriFlux BASE data pipeline to support

https://doi.org/10.5194/essd-2026-732
Preprint. Discussion started: 2 November 2026
© Author(s) 2026. CC BY 4.0 License.



network growth and data sharing, Sci. Data, 10, 614, 10.1038/s41597-023-02531-2, 2023.

Chu, H., Luo, X., Ouyang, Z., Chan, W. S., Dengel, S., Biraud, S. C., Torn, M. S., Metzger, S., Kumar, J., Arain, M. A., Arkebauer, T. J., Baldocchi, D., Bernacchi, C., Billesbach, D., Black, T. A., Blanken, P. D., Bohrer, G., Bracho, R., Brown, S., Brunsell, N. A., Chen, J., Chen, X., Clark, K., Desai, A. R., Duman, T., Durden, D., Fares, S., Forbrich, I., Gamon, J. A., Gough, C. M., Griffis, T., Helbig, M., Hollinger, D., Humphreys, E., Ikawa, H., Iwata, H., Ju, Y., Knowles, J. F., Knox, S. H., Kobayashi, H., Kolb, T., Law, B., Lee, X., Litvak, M., Liu, H., Munger, J. W., Noormets, A., Novick, K., Oberbauer, S. F., Oechel, W., Oikawa, P., Papuga, S. A., Pendall, E., Prajapati, P., Prueger, J., Quinton, W. L., Richardson, A. D., Russell, E. S., Scott, R. L., Starr, G., Staebler, R., Stoy, P. C., Stuart-Haëntjens, E., Sonnentag, O., Sullivan, R. C., Suyker, A., Ueyama, M., Vargas, R., Wood, J. D., and Zona, D.: Representativeness of Eddy-Covariance flux footprints for areas surrounding AmeriFlux sites, Agric. For. Meteorol., 301-302, 108350, https://doi.org/10.1016/j.agrformet.2021.108350, 2021.

Copernicus Climate Change, S.: Land cover classification gridded maps from 1992 to present derived from satellite observations, https://doi.org/10.24381/cds.006f2c9a, 2019.

Cui, Y., Jia, L., and Fan, W.: Estimation of actual evapotranspiration and its components in an irrigated area by integrating the Shuttleworth-Wallace and surface temperature-vegetation index schemes using the particle swarm optimization algorithm, Agric. For. Meteorol., 307, 108488, https://doi.org/10.1016/j.agrformet.2021.108488, 2021.

De Kauwe, M. G., Medlyn, B. E., Knauer, J., and Williams, C. A.: Ideas and perspectives: how coupled is the vegetation to the boundary layer?, Biogeosciences, 14, 4435-4453, https://doi.org/10.5194/bg-14-4435-2017, 2017.

De Kauwe, M. G., Kala, J., Lin, Y. S., Pitman, A. J., Medlyn, B. E., Duursma, R. A., Abramowitz, G., Wang, Y. P., and Miralles, D. G.: A test of an optimal stomatal conductance scheme within the CABLE land surface model, Geosci. Model Dev., 8, 431-452, https://doi.org/10.5194/gmd-8-431-2015, 2015.

https://doi.org/10.5194/essd-2026-732
Preprint. Discussion started: 2 November 2026
© Author(s) 2026. CC BY 4.0 License.



727 Di, S.-C., Li, Z.-L., Ren, Y., Liu, M., Jiang, Y.-Z., Zheng, F.-D., Li, X.-M., Qi, Y.-B., Liu, H.-L.,
728 and Tang, R.: Estimation of Regional Evapotranspiration Based on the Decouple Model and
729 Remote Sensing Information ——a Case Study in Beijing City and Nearby Region, Int. J.
730 Remote Sens., 45, 7753-7774, 10.1080/01431161.2024.2316674, 2024.
731 Dickinson, R. E.: Modeling evapotranspiration for three-dimensional global climate models,
732 Climate processes and climate sensitivity, 29, 58-72, https://doi.org/10.1029/GM029p0058,
733 1984.
734 Dirmeyer, P. A.: The terrestrial segment of soil moisture–climate coupling, Geophys. Res. Lett., 38,
735 https://doi.org/10.1029/2011GL048268, 2011.
736 Eyring, V., Collins, W. D., Gentine, P., Barnes, E. A., Barreiro, M., Beucler, T., Bocquet, M.,
737 Bretherton, C. S., Christensen, H. M., Dagon, K., Gagne, D. J., Hall, D., Hammerling, D.,
738 Hoyer, S., Iglesias-Suarez, F., Lopez-Gomez, I., McGraw, M. C., Meehl, G. A., Molina, M. J.,
739 Monteleoni, C., Mueller, J., Pritchard, M. S., Rolnick, D., Runge, J., Stier, P., Watt-Meyer, O.,
740 Weigel, K., Yu, R., and Zanna, L.: Pushing the frontiers in climate modelling and analysis
741 with machine learning, Nat. Clim. Change, 14, 916-928, 10.1038/s41558-024-02095-y, 2024.
742 ElGhawi, R., Kraft, B., Reimers, C., Reichstein, M., Körner, M., Gentine, P., and Winkler, A. J.:
743 Hybrid modeling of evapotranspiration: inferring stomatal and aerodynamic resistances using
744 combined physics-based and machine learning, Environ. Res. Lett., 18, 034039,
745 https://doi.org/10.1088/1748-9326/acbbe0, 2023.
746 Fang, H., Baret, F., Plummer, S., and Schaepman-Strub, G.: An Overview of Global Leaf Area
747 Index (LAI): Methods, Products, Validation, and Applications, Rev. Geophys., 57, 739-799,
748 https://doi.org/10.1029/2018RG000608, 2019.
749 Feng, J., Zhang, K., Chao, L., Zhan, H., and Li, Y.: P-LSHv2: a multi-decadal global daily
750 evapotranspiration dataset enhanced with explicit soil moisture constraints, Earth Syst. Sci.
751 Data, 17, 5039-5064, https://doi.org/10.5194/essd-17-5039-2025, 2025.
752 Feng, Y., Gong, D. Z., Mei, X. R., Hao, W. P., Tang, D. H., and Cui, N. B.: Energy balance and

https://doi.org/10.5194/essd-2026-732
Preprint. Discussion started: 2 November 2026
© Author(s) 2026. CC BY 4.0 License.



753 partitioning in partial plastic mulched and non-mulched maize fields on the Loess Plateau of
754 China, Agric. Water Manage., 191, 193-206, https://doi.org/10.1016/j.agwat.2017.06.009,
755 2017.
756 Feng, Y., Hao, W. P., Gao, L. L., Li, H. R., Gong, D. Z., and Cui, N. B.: Comparison of maize water
757 consumption at different scales between mulched and non-mulched croplands, Agric. Water
758 Manage., 216, 315-324, https://doi.org/10.1016/j.agwat.2019.02.016, 2019.
759 Fisher, J. B., Malhi, Y., Bonal, D., Da Rocha, H. R., De AraÚJo, A. C., Gamo, M., Goulden, M. L.,
760 Hirano, T., Huete, A. R., Kondo, H., Kumagai, T. O., Loescher, H. W., Miller, S., Nobre, A.
761 D., Nouvellon, Y., Oberbauer, S. F., Panuthai, S., Roupsard, O., Saleska, S., Tanaka, K.,
762 Tanaka, N., Tu, K. P., and Von Randow, C.: The land–atmosphere water flux in the tropics,
763 Global Change Biol., 15, 2694-2714, https://doi.org/10.1111/j.1365-2486.2008.01813.x, 2009.
764 Gentine, P., Entekhabi, D., Chehbouni, A., Boulet, G., and Duchemin, B.: Analysis of evaporative
765 fraction diurnal behaviour, Agric. For. Meteorol., 143, 13-29,
766 https://doi.org/10.1016/j.agrformet.2006.11.002, 2007.
767 Good, S. P., Noone, D., and Bowen, G.: Hydrologic connectivity constrains partitioning of global
768 terrestrial water fluxes, Science, 349, 175-177, https://doi.org/10.1126/science.aaa5931, 2015.
769 Grossiord, C., Buckley, T. N., Cernusak, L. A., Novick, K. A., Poulter, B., Siegwolf, R. T. W.,
770 Sperry, J. S., and McDowell, N. G.: Plant responses to rising vapor pressure deficit, New
771 Phytol., 226, 1550-1566, https://doi.org/10.1111/nph.16485, 2020.
772 Gupta, S., Lehmann, P., Bickel, S., Bonetti, S., and Or, D.: Global Mapping of Potential and
773 Climatic Plant-Available Soil Water, Journal of Advances in Modeling Earth Systems, 15,
774 e2022MS003277, https://doi.org/10.1029/2022MS003277, 2023.
775 Han, S., Yan, J., Liu, Y., Tian, F., Zhang, B., Wang, X., Shao, C., and Wang, L.: Contrasting Land
776 and Atmospheric Controls on the Generalized Complementary Relationship of Evaporation
777 Over Grasslands and Forests, Water Resour. Res., 59, e2023WR035501,
778 https://doi.org/10.1029/2023WR035501, 2023.

https://doi.org/10.5194/essd-2026-732
Preprint. Discussion started: 2 November 2026
© Author(s) 2026. CC BY 4.0 License.



779 Haynes, K., Lagerquist, R., McGraw, M., Musgrave, K., and Ebert-Uphoff, I.: Creating and
780 Evaluating Uncertainty Estimates with Neural Networks for Environmental-Science
781 Applications, Artificial Intelligence for the Earth Systems, 2, 220061,
782 https://doi.org/10.1175/AIES-D-22-0061.1, 2023.
783 Hersbach, H., Bell, B., Berrisford, P., Hirahara, S., Horányi, A., Muñoz-Sabater, J., Nicolas, J.,
784 Peubey, C., Radu, R., and Schepers, D.: The ERA5 global reanalysis, Q. J. R. Meteorolog.
785 Soc., 146, 1999-2049, https://doi.org/10.1002/qj.3803, 2020.
786 Huang, L., Luo, Y., Chen, J. M., Tang, Q., Steenhuis, T., Cheng, W., and Shi, W.: Satellite-based
787 near-real-time global daily terrestrial evapotranspiration estimates, Earth Syst. Sci. Data, 16,
788 3993-4019, 10.5194/essd-16-3993-2024, 2024.
789 Jarvis, P.: The interpretation of the variations in leaf water potential and stomatal conductance
790 found in canopies in the field, Philosophical Transactions of the Royal Society of London. B,
791 Biological Sciences, 273, 593-610, https://doi.org/10.1098/rstb.1976.0035, 1976.
792 Jarvis, P. G. and McNaughton, K. G.: Stomatal control of transpiration: Scaling up from leaf to
793 region, Adv. Ecol. Res., 15, 1-49, https://doi.org/10.1016/S0065-2504(08)60119-1, 1986.
794 Jiang, S., Wu, J., Wang, Z., He, Z., Wang, M., Yao, W., and Feng, Y.: Spatiotemporal variations of
795 cropland carbon sequestration and water loss across China, Agric. Water Manage., 287,
796 108427, https://doi.org/10.1016/j.agwat.2023.108427, 2023.
797 Jung, M., Koirala, S., Weber, U., Ichii, K., Gans, F., Camps-Valls, G., Papale, D., Schwalm, C.,
798 Tramontana, G., and Reichstein, M.: The FLUXCOM ensemble of global land-atmosphere
799 energy fluxes, Sci. Data, 6, 74, https://doi.org/10.1038/s41597-019-0076-8, 2019.
800 Jung, M., Reichstein, M., Ciais, P., Seneviratne, S. I., Sheffield, J., Goulden, M. L., Bonan, G.,
801 Cescatti, A., Chen, J., de Jeu, R., Dolman, A. J., Eugster, W., Gerten, D., Gianelle, D., Gobron,
802 N., Heinke, J., Kimball, J., Law, B. E., Montagnani, L., Mu, Q., Mueller, B., Oleson, K.,
803 Papale, D., Richardson, A. D., Roupsard, O., Running, S., Tomelleri, E., Viovy, N., Weber, U.,
804 Williams, C., Wood, E., Zaehle, S., and Zhang, K.: Recent decline in the global land

https://doi.org/10.5194/essd-2026-732
Preprint. Discussion started: 2 November 2026
© Author(s) 2026. CC BY 4.0 License.



evapotranspiration trend due to limited moisture supply, Nature, 467, 951-954, 10.1038/nature09396, 2010.

Kang, Y., Bassiouni, M., Gaber, M., Lu, X., and Keenan, T. F.: CEDAR-GPP: spatiotemporally upscaled estimates of gross primary productivity incorporating CO2 fertilization, Earth Syst. Sci. Data, 17, 3009-3046, https://doi.org/10.5194/essd-17-3009-2025, 2025.

Kannenberg, S. A., Anderegg, W. R. L., Barnes, M. L., Dannenberg, M. P., and Knapp, A. K.: Dominant role of soil moisture in mediating carbon and water fluxes in dryland ecosystems, Nat. Geosci., 17, 38-43, https://doi.org/10.1038/s41561-023-01351-8, 2024.

Knauer, J., El-Madany, T. S., Zaehle, S., and Migliavacca, M.: Bigleaf—An R package for the calculation of physical and physiological ecosystem properties from eddy covariance data, PLoS One, 13, e0201114, https://doi.org/10.1371/journal.pone.0201114, 2018.

Leng, J., Chen, J. M., Li, W., Luo, X., Xu, M., Liu, J., Wang, R., Rogers, C., Li, B., and Yan, Y.: Global datasets of hourly carbon and water fluxes simulated using a satellite-based process model with dynamic parameterizations, Earth Syst. Sci. Data, 16, 1283-1300, https://doi.org/10.5194/essd-16-1283-2024, 2024.

Leuning, R., van Gorsel, E., Massman, W. J., and Isaac, P. R.: Reflections on the surface energy imbalance problem, Agric. For. Meteorol., 156, 65-74, https://doi.org/10.1016/j.agrformet.2011.12.002, 2012.

Li, S., Wang, G., Sun, S., Chen, Z., Mura, M., Lu, J., Liu, Q., Li, J., Hagan, D. F. T., García-García, A., and Peng, J.: Observed declining strength of vegetation-atmosphere coupling, Agric. For. Meteorol., 379, 111051, https://doi.org/10.1016/j.agrformet.2026.111051, 2026.

Lian, X., Jeong, S., Park, C.-E., Xu, H., Li, L. Z. X., Wang, T., Gentine, P., Peñuelas, J., and Piao, S.: Biophysical impacts of northern vegetation changes on seasonal warming patterns, Nat. Commun., 13, 3925, https://doi.org/10.1038/s41467-022-31671-z, 2022.

Lin, Z., Feng, Y., Wu, J., Gong, D., Xiong, J., Cao, X., and Zheng, C.: Data-driven attribution of evapotranspiration dynamics in the Heihe River Basin: Controlling factors from site

https://doi.org/10.5194/essd-2026-732
Preprint. Discussion started: 2 November 2026
© Author(s) 2026. CC BY 4.0 License.



measurements to regional satellite observations, Agric. Water Manage., 328, 110324, https://doi.org/10.1016/j.agwat.2026.110324, 2026.

Maurer, K. D., Bohrer, G., Kenny, W. T., and Ivanov, V. Y.: Large-eddy simulations of surface roughness parameter sensitivity to canopy-structure characteristics, Biogeosciences, 12, 2533-2548, 10.5194/bg-12-2533-2015, 2015.

McNaughton, K. G. and Jarvis, P. G.: Effects of spatial scale on stomatal control of transpiration, Agric. For. Meteorol., 54, 279-302, https://doi.org/10.1016/0168-1923(91)90010-N, 1991.

Medlyn, B. E., Duursma, R. A., Eamus, D., Ellsworth, D. S., Prentice, I. C., Barton, C. V., Crous, K. Y., De Angelis, P., Freeman, M., and Wingate, L.: Reconciling the optimal and empirical approaches to modelling stomatal conductance, Global Change Biol., 17, 2134-2144, https://doi.org/10.1111/j.1365-2486.2010.02375.x, 2011.

Mehrez, M. B., Taconet, O., Vidal-Madjar, D., and Valencogne, C.: Estimation of stomatal resistance and canopy evaporation during the HAPEX-MOBILHY experiment, Agric. For. Meteorol., 58, 285-313, https://doi.org/10.1016/0168-1923(92)90066-D, 1992.

Miralles, D. G., Bonte, O., Koppa, A., Baez-Villanueva, O. M., Tronquo, E., Zhong, F., Beck, H. E., Hulsman, P., Dorigo, W., Verhoest, N. E. C., and Haghdoost, S.: GLEAM4: global land evaporation and soil moisture dataset at 0.1° resolution from 1980 to near present, Sci. Data, 12, 416, https://doi.org/10.1038/s41597-025-04610-y, 2025.

Monteith, J. L. and Unsworth, M. H.: Chapter 13 - Steady-State Heat Balance: (i) Water Surfaces, Soil, and Vegetation, in: Principles of Environmental Physics (Fourth Edition), edited by: Monteith, J. L., and Unsworth, M. H., Academic Press, Boston, 217-247, https://doi.org/10.1016/B978-0-12-386910-4.00013-5, 2013.

Mu, Q., Zhao, M., and Running, S. W.: Algorithm Theoretical Basis Document, Collection, 5, 381-394, https://scholarworks.umt.edu/ntsg_pubs/268/, 2013.

Noilhan, J. and Planton, S.: A simple parameterization of land surface processes for meteorological models, Mon. Weather Rev., 117, 536-549, https://doi.org/10.1175/1520-

https://doi.org/10.5194/essd-2026-732
Preprint. Discussion started: 2 November 2026
© Author(s) 2026. CC BY 4.0 License.



0493(1989)117<0536:ASPOLS>2.0.CO;2, 1989.

Novick, K. A., Ficklin, D. L., Stoy, P. C., Williams, C. A., Bohrer, G., Oishi, A. C., Papuga, S. A., Blanken, P. D., Noormets, A., and Sulman, B. N.: The increasing importance of atmospheric demand for ecosystem water and carbon fluxes, Nat. Clim. Change, 6, 1023-1027, https://doi.org/10.1038/nclimate3114, 2016.

Papale, D., Reichstein, M., Aubinet, M., Canfora, E., Bernhofer, C., Kutsch, W., Longdoz, B., Rambal, S., Valentini, R., Vesala, T., and Yakir, D.: Towards a standardized processing of Net Ecosystem Exchange measured with eddy covariance technique: algorithms and uncertainty estimation, Biogeosciences, 3, 571-583, https://doi.org/10.5194/bg-3-571-2006, 2006.

Pastorello, G., Trotta, C., Canfora, E., Chu, H., Christianson, D., Cheah, Y.-W., Poindexter, C., Chen, J., Elbashandy, A., and Humphrey, M.: The FLUXNET2015 dataset and the ONEFlux processing pipeline for eddy covariance data, Sci. Data, 7, 225, https://doi.org/10.1038/s41597-020-0534-3, 2020.

Pétron, G., Handley, P., Hakala, J., Kofler, J., Thoning, K. W., Crotwell, A., Clarke, A., Fernandez, J., Crocker, I., Burgener, R., Thomas, B., Colton, A., Jordan, S., Longren, L., Doneghey, M., Trudeau, M., Mefford, T., DeVogel, S., Searle, A., Lan, X., Mauss, J., Smith, C., Vasel, B., Morris, S., Miller, J., and Mund, J.: Atmospheric Carbon Dioxide Dry Air Mole Fractions from continuous measurements at Mauna Loa, Hawaii, Utqiaġvik, Alaska, American Samoa and South Pole, 1973–present, NOAA Global Monitoring Laboratory, https://doi.org/10.15138/yaf1-bk21, 2026.

Peng, L., Zeng, Z., Wei, Z., Chen, A., Wood, E. F., and Sheffield, J.: Determinants of the ratio of actual to potential evapotranspiration, Global Change Biol., 25, 1326-1343, https://doi.org/10.1111/gcb.14577, 2019.

Potapov, P., Li, X., Hernandez-Serna, A., Tyukavina, A., Hansen, M. C., Kommareddy, A., Pickens, A., Turubanova, S., Tang, H., and Silva, C. E.: Mapping global forest canopy height through integration of GEDI and Landsat data, Remote Sens. Environ., 253, 112165,

https://doi.org/10.5194/essd-2026-732
Preprint. Discussion started: 2 November 2026
© Author(s) 2026. CC BY 4.0 License.



https://doi.org/10.1016/j.rse.2020.112165, 2021.

Quets, J., De Lannoy, G. J. M., Al Yaari, A., Chan, S., Cosh, M. H., Gruber, A., Reichle, R. H., Van der Schalie, R., and Wigneron, J.-P.: Uncertainty in soil moisture retrievals: An ensemble approach using SMOS L-band microwave data, Remote Sens. Environ., 229, 133-147, https://doi.org/10.1016/j.rse.2019.05.008, 2019.

Reichstein, M., Camps-Valls, G., Stevens, B., Jung, M., Denzler, J., Carvalhais, N., and Prabhat: Deep learning and process understanding for data-driven Earth system science, Nature, 566, 195-204, https://doi.org/10.1038/s41586-019-0912-1, 2019.

Sellers, P. J., Mintz, Y., Sud, Y. e. a., and Dalcher, A.: A simple biosphere model (SiB) for use within general circulation models, Journal of Atmospheric Sciences, 43, 505-531, https://doi.org/10.1175/1520-0469(1986)043<0505:ASBMFU>2.0.CO;2, 1986.

Shen, C., Appling, A. P., Gentine, P., Bandai, T., Gupta, H., Tartakovsky, A., Baity-Jesi, M., Fenicia, F., Kifer, D., Li, L., Liu, X., Ren, W., Zheng, Y., Harman, C. J., Clark, M., Farthing, M., Feng, D., Kumar, P., Aboelyazeed, D., Rahmani, F., Song, Y., Beck, H. E., Bindas, T., Dwivedi, D., Fang, K., Höge, M., Rackauckas, C., Mohanty, B., Roy, T., Xu, C., and Lawson, K.: Differentiable modelling to unify machine learning and physical models for geosciences, Nature Reviews Earth & Environment, 4, 552-567, 10.1038/s43017-023-00450-9, 2023.

Stewart, J. B.: Modelling surface conductance of pine forest, Agric. For. Meteorol., 43, 19-35, https://doi.org/10.1016/0168-1923(88)90003-2, 1988.

Stoy, P. C., Mauder, M., Foken, T., Marcolla, B., Boegh, E., Ibrom, A., Arain, M. A., Arneth, A., Aurela, M., Bernhofer, C., Cescatti, A., Dellwik, E., Duce, P., Gianelle, D., van Gorsel, E., Kiely, G., Knohl, A., Margolis, H., McCaughey, H., Merbold, L., Montagnani, L., Papale, D., Reichstein, M., Saunders, M., Serrano-Ortiz, P., Sottocornola, M., Spano, D., Vaccari, F., and Varlagin, A.: A data-driven analysis of energy balance closure across FLUXNET research sites: The role of landscape scale heterogeneity, Agric. For. Meteorol., 171-172, 137-152, https://doi.org/10.1016/j.agrformet.2012.11.004, 2013.

https://doi.org/10.5194/essd-2026-732
Preprint. Discussion started: 2 November 2026
© Author(s) 2026. CC BY 4.0 License.



909 Tavakoli, N. and Dirmeyer, P. A.: A global dataset of land-atmosphere coupling metrics based on
910 observations for evaluating Earth system models, Sci. Data, https://doi.org/10.1038/s41597-
911 026-07519-2, 2026.
912 Tramontana, G., Jung, M., Schwalm, C. R., Ichii, K., Camps-Valls, G., Ráduly, B., Reichstein, M.,
913 Arain, M. A., Cescatti, A., Kiely, G., Merbold, L., Serrano-Ortiz, P., Sickert, S., Wolf, S., and
914 Papale, D.: Predicting carbon dioxide and energy fluxes across global FLUXNET sites with
915 regression algorithms, Biogeosciences, 13, 4291-4313, https://doi.org/10.5194/bg-13-4291-
916 2016, 2016.
917 Wu, Y., Miao, C., Wang, Y., Zhang, Q., Ji, J., and Chai, Y.: Multi-spatial scale assessment and multi-
918 dataset fusion of global terrestrial evapotranspiration datasets, Earth Syst. Sci. Data, 17, 6445-
919 6460, https://doi.org/10.5194/essd-17-6445-2025, 2025.
920 Xia, H., Zhang, F., Ciais, P., Stoy, P. C., Peñuelas, J., Lian, X., Wang, Y.-P., Makowski, D., Luo, Y.,
921 Niu, S., Yu, G., Huang, J., Wang, X., Zahn, E., and Fu, Z.: Higher optimal temperature for
922 vegetation transpiration than for photosynthesis, Nat. Plants, 12, 703-718,
923 https://doi.org/10.1038/s41477-026-02263-2, 2026.
924 Xiao, J., Baldocchi, D., Ichii, K., Li, F., and Papale, D.: Insights into terrestrial carbon and water
925 cycling from the global eddy covariance network, Nature Reviews Earth & Environment, 7,
926 60-79, https://doi.org/10.1038/s43017-025-00743-1, 2026.
927 Xiong, J. and Feng, Y.: A long-term gridded dataset of vegetation–atmosphere decoupling
928 coefficient across the contiguous United States, 1982–2020, Zenodo [data set],
929 https://doi.org/10.5281/zenodo.21670853, 2026.
930 Yang, Y., Roderick, M. L., Guo, H., Miralles, D. G., Zhang, L., Fatichi, S., Luo, X., Zhang, Y.,
931 McVicar, T. R., Tu, Z., Keenan, T. F., Fisher, J. B., Gan, R., Zhang, X., Piao, S., Zhang, B.,
932 and Yang, D.: Evapotranspiration on a greening Earth, Nature Reviews Earth & Environment,
933 4, 626-641, https://doi.org/10.1038/s43017-023-00464-3, 2023.
934 Yao, Y., Liang, S., and Xie, Z.: Chapter 80 - GLASS MODIS (1km, 2000–2020) and AVHRR (0.05°,

https://doi.org/10.5194/essd-2026-732
Preprint. Discussion started: 2 November 2026
© Author(s) 2026. CC BY 4.0 License.



1981–2020) 8-day ET products, Handbook of Satellite Land Products, 645-649, https://doi.org/10.1016/B978-0-443-21485-1.00080-7, 2026.

Zha, T., Li, C., Kellomäki, S., Peltola, H., Wang, K.-Y., and Zhang, Y.: Controls of Evapotranspiration and CO2 Fluxes from Scots Pine by Surface Conductance and Abiotic Factors, PLoS One, 8, e69027, https://doi.org/10.1371/journal.pone.0069027, 2013.

Zhang, Y., Narayanappa, D., Ciais, P., Li, W., Goll, D., Vuichard, N., De Kauwe, M. G., Li, L., and Maignan, F.: Evaluating the vegetation–atmosphere coupling strength of ORCHIDEE land surface model (v7266), Geosci. Model Dev., 15, 9111-9125, https://doi.org/10.5194/gmd-15-9111-2022, 2022.

Zhao, W. L., Gentine, P., Reichstein, M., Zhang, Y., Zhou, S., Wen, Y., Lin, C., Li, X., and Qiu, G. Y.: Physics-Constrained Machine Learning of Evapotranspiration, Geophys. Res. Lett., 46, 14496-14507, https://doi.org/10.1029/2019GL085291, 2019.

https://doi.org/10.5194/essd-2026-732
Preprint. Discussion started: 2 November 2026
© Author(s) 2026. CC BY 4.0 License.



Open Access Earth System Science Data Discussions

947 **Table 1. Major uncertainty sources and their treatment in the CONUS gridded Ω product.**
948 Quantified components are partly represented by Monte Carlo or ensemble spread, whereas
949 diagnosed components are characterized by validation statistics or quality-control indicators. The
950 reported uncertainty does not represent the total uncertainty of the product.

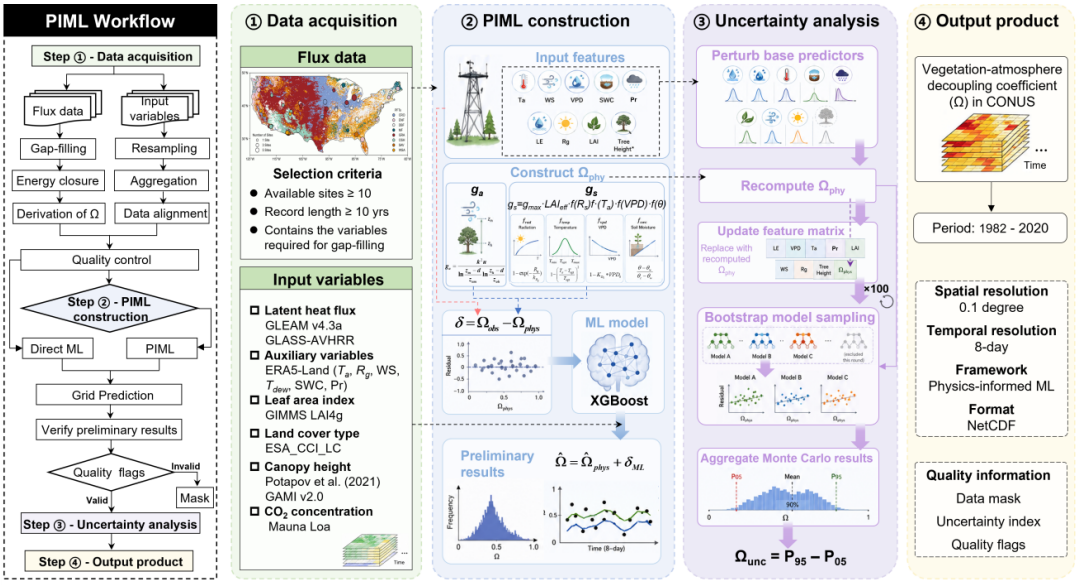
Uncertainty source	Main cause	Treatment
EC-derived Ω	Measurement, processing, and gap-filling errors	Energy closure balance, Physical-range filtering
Input predictors and scale mismatch	Source-data errors and mismatch between EC footprints and 0.1° grids	Data harmonization, range checks, PFT-consistent matching, and Monte Carlo perturbation
Model uncertainty	Limited training data and model structural assumptions	Site-level cross-validation, model comparison, and Monte Carlo perturbation
Feature extrapolation	Predictor combinations outside the tower-observed domain	Out-of-range metrics, extrapolation-risk assessment, and physical constraints
Temporal reconstruction	Limited temporal overlap between EC observations and the 1982–2020 reconstruction	Annual QC assessment and temporal-consistency analysis
Missingness and clipping	Missing predictors and range enforcement	Missing-value records, clipping flags, and valid-fraction statistics

951

https://doi.org/10.5194/essd-2026-732
Preprint. Discussion started: 2 November 2026
© Author(s) 2026. CC BY 4.0 License.

Open Access Earth System Science Data Discussions

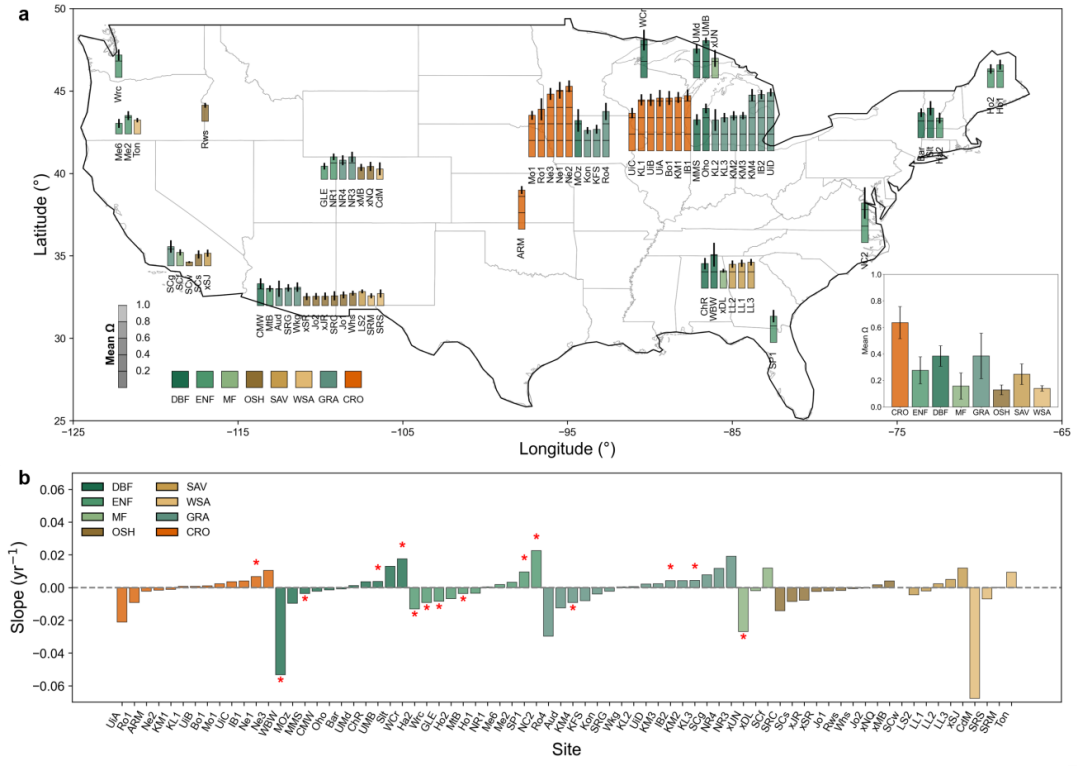
952 **Figure 1. Workflow for generating the CONUS Ω data product.**



953

https://doi.org/10.5194/essd-2026-732
Preprint. Discussion started: 2 November 2026
© Author(s) 2026. CC BY 4.0 License.

Figure 2. Spatial distribution, site-level mean Ω, and temporal trends across flux-tower sites. **(a)** Spatial distribution of the flux-tower sites used to derive and evaluate site-level Ω across CONUS. Each vertical bar represents the mean Ω at an individual site, with bar color indicating PFT: deciduous broadleaf forest (DBF), evergreen needleleaf forest (ENF), mixed forest (MF), open shrubland (OSH), savanna (SAV), woody savanna (WSA), grassland (GRA), and cropland (CRO). Error bars indicate site-level variability in Ω. The inset summarizes mean Ω by PFT, with bars showing the PFT mean and error bars showing among-site variability. **(b)** Site-level linear trends in Ω, sorted by PFT group. Bars show the slope of Ω over time for each site. The dashed horizontal line indicates zero trend. Red "*" denote statistically significant trends ($p < 0.05$). Site labels are abbreviated by removing the "US-" prefix.



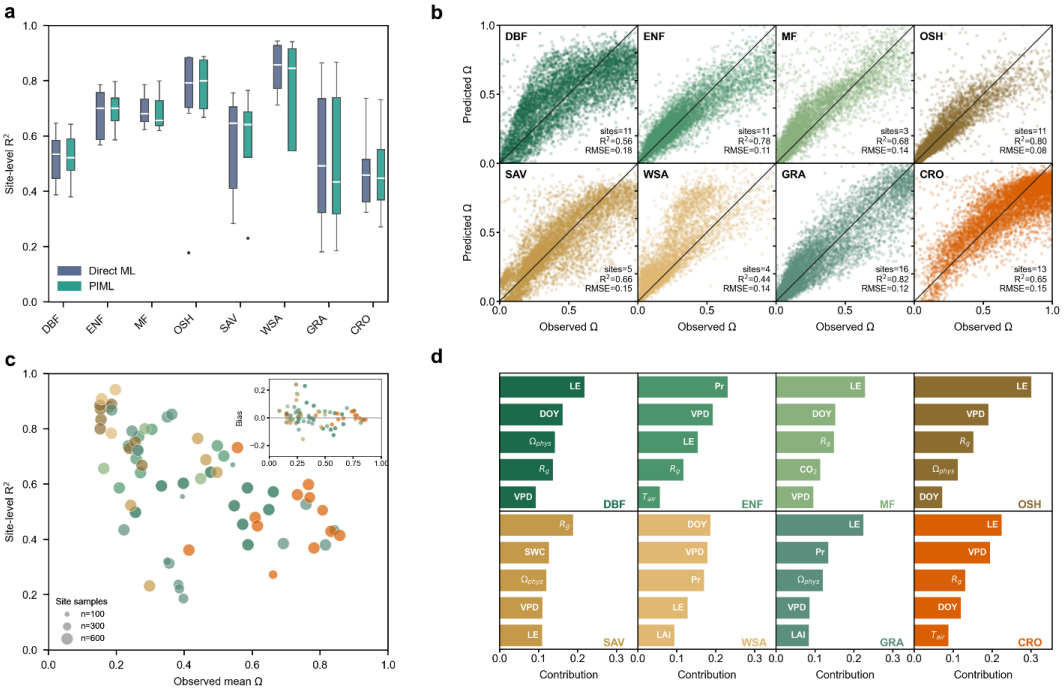
https://doi.org/10.5194/essd-2026-732
Preprint. Discussion started: 2 November 2026
© Author(s) 2026. CC BY 4.0 License.



Open Access Earth System Science Data Discussions

Figure 3. Site-independent validation of the PIML framework.

(a) PFT-specific site-level validation skill for Direct ML and PIML under site-blocked cross-validation, where entire sites were withheld during testing. Boxes summarize the distribution of site-level R^2 across held-out sites; the white line indicates the median. **(b)** Observed versus predicted Ω for PIML across the eight PFTs. Each point represents 8-day site observation, and the dashed line indicates the 1:1 relationship. Reported R^2 and RMSE values were calculated from pooled out-of-fold predictions within each PFT. **(c)** Relationship between site-level R^2 and observed mean Ω, with point color denoting PFT and point size proportional to the number of valid observations. The inset shows site-level mean prediction bias as a function of observed mean Ω. **(d)** Top predictor contributions for each PFT-specific PIML model. Bars show the five most influential predictors within each PFT, with labels placed inside bars.

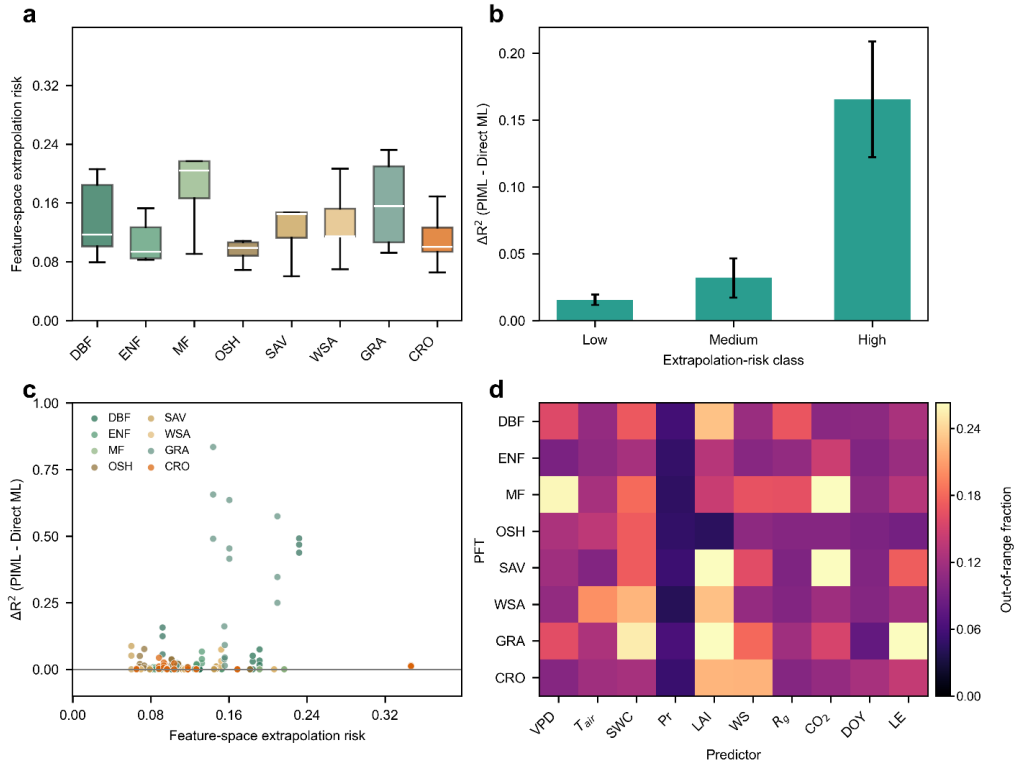


https://doi.org/10.5194/essd-2026-732
Preprint. Discussion started: 2 November 2026
© Author(s) 2026. CC BY 4.0 License.



Open Access Earth System Science Data Discussions

977 **Figure 4. Feature-space extrapolation risk and PIML improvement relative to Direct ML.**
978 **(a)** Distribution of held-out feature-space extrapolation risk by PFT. Extrapolation risk was defined
979 as the fraction of predictor values in held-out test sites that fell outside the 5th-95th percentile range
980 (departure from the well-sampled part of the training distribution) of the corresponding training
981 sites within the same PFT and split. **(b)** Mean R^2 improvement of PIML relative to Direct ML
982 across low-, medium-, and high-risk validation cases. Low-, medium-, and high-risk groups were
983 defined by tertiles of extrapolation risk across all PFT-split-model combinations. Error bars indicate
984 the standard error across PFT-split-model combinations. **(c)** Relationship between feature-space
985 extrapolation risk and R^2 improvement, where each point represents a PFT-split-model combination
986 and colors denote PFTs. **(d)** Predictor-level out-of-range fraction by PFT, indicating which
987 environmental or biophysical covariates contributed most strongly to extrapolation risk.



988

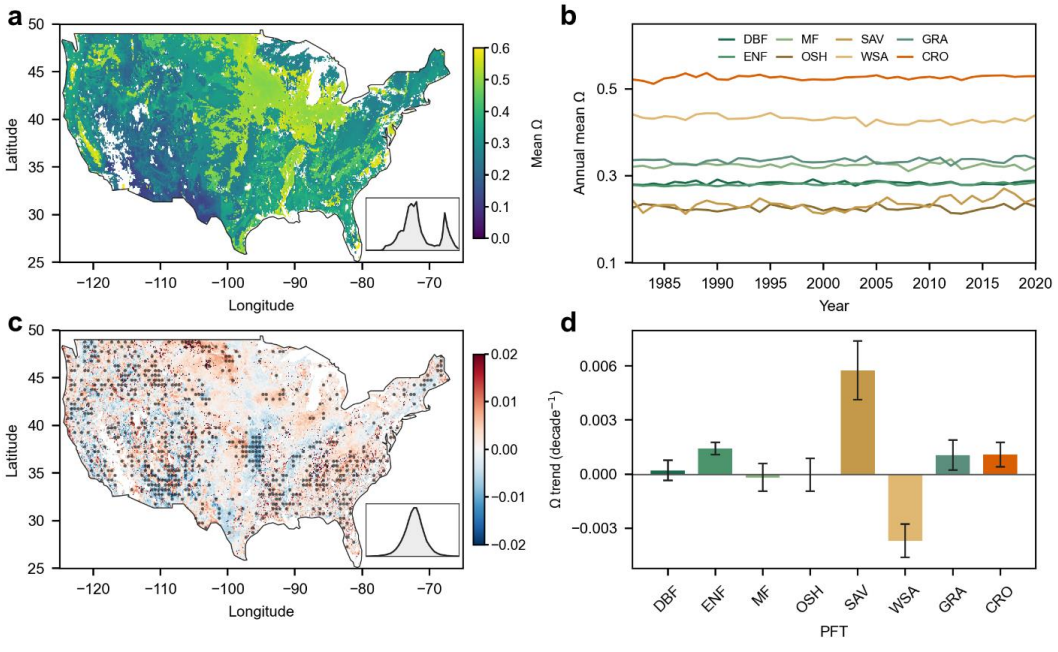
https://doi.org/10.5194/essd-2026-732
Preprint. Discussion started: 2 November 2026
© Author(s) 2026. CC BY 4.0 License.



Open Access Earth System Science Data Discussions

989 **Figure 5. Spatial patterns and temporal changes.**

990 **(a)** Mean annual Ω across the CONUS gridded product. The lower-right insets show the
991 distributions of valid grid-cell values within the displayed color ranges. **(b)** Annual Ω time series
992 across PFTs. Lines indicate annual means for each PFT. **(c)** Pixel-level linear trend in Ω. Stippling
993 denotes trends significant at $p < 0.05$ based on Mann–Kendall test; points are displayed every fifth
994 grid cell for clarity. **(d)** PFT-level Ω trends. Bars show the trend slopes, and error bars show one
995 standard error of the slope.



996

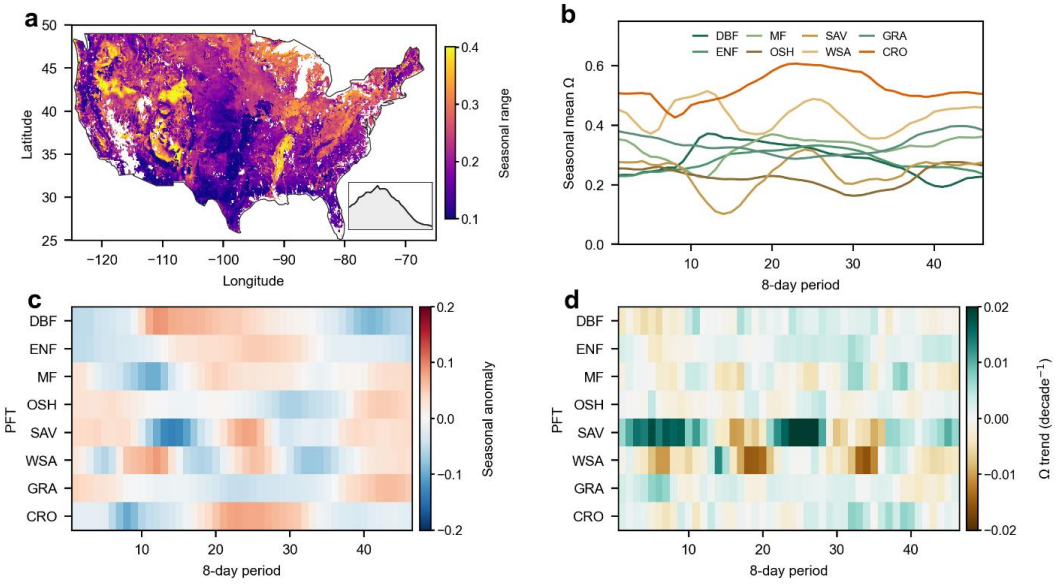
https://doi.org/10.5194/essd-2026-732
Preprint. Discussion started: 2 November 2026
© Author(s) 2026. CC BY 4.0 License.



Open Access Earth System Science Data Discussions

997 **Figure 6. Seasonality variation and period-specific long-term trends in Ω.**

998 **(a)** Spatial pattern of Ω seasonal range, calculated as the difference between the maximum and
999 minimum means across all 46 8-day periods of the year. **(b)** PFT-level mean seasonal cycles of Ω
1000 across 8-day periods. **(c)** PFT-by-season heatmap of Ω seasonal anomalies, showing deviations
1001 from each PFT mean seasonal state. **(d)** PFT-by-season heatmap of long-term Ω trends from 1982
1002 to 2020 for each 8-day period.



1003

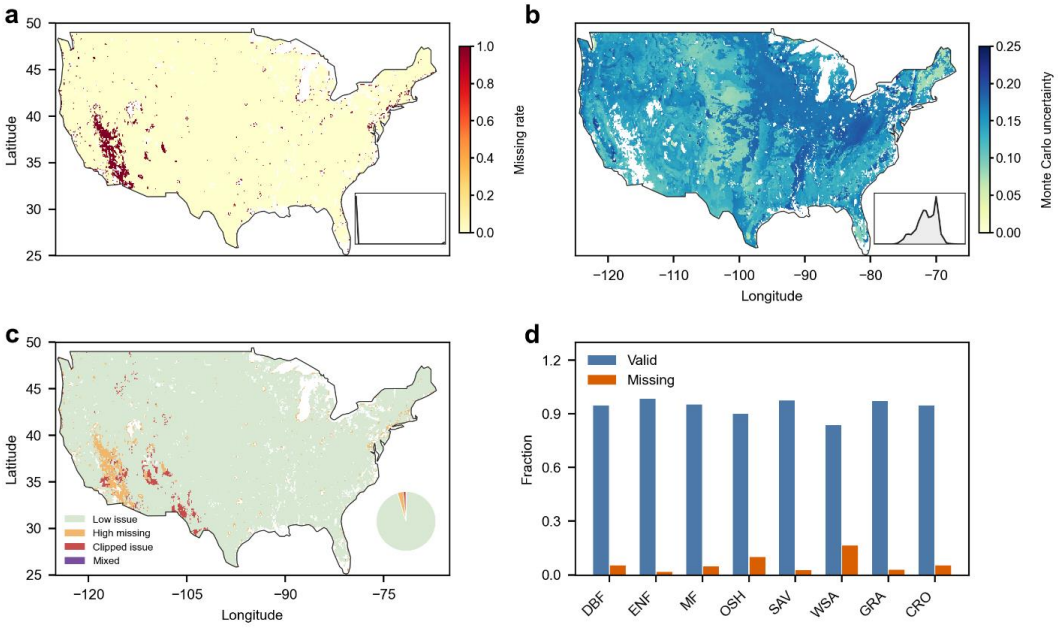
https://doi.org/10.5194/essd-2026-732
Preprint. Discussion started: 2 November 2026
© Author(s) 2026. CC BY 4.0 License.



Open Access Earth System Science Data Discussions

1004 **Figure 7. Product quality, uncertainty, and quality-control diagnostics.**

1005 **(a)** Spatial distribution of the missing rate, calculated for each target grid cell as the fraction of
1006 missing or invalid estimates among all 8-day layers from 1982 to 2020. **(b)** Mean Monte Carlo
1007 uncertainty of Ω across CONUS, derived from the uncertainty ensemble. **(c)** Spatial distribution of
1008 quality-control classes. "Low issue" indicates target grid cells with missing rate < 0.30 and pre-
1009 clipping outside-rate < 0.01; "High missing" indicates missing rate ≥ 0.30; "Clipped issue"
1010 indicates pre-clipping outside-rate ≥ 0.01; and "Mixed" indicates grid cells satisfying both missing-
1011 prone and clipped-prone criteria. **(d)** PFT-level summary of valid and missing product fractions.



1012